

DIAMOND FILMS and DEVICES

Chemistry, Electronics and Mechanics

Venkatesh Seshan

Diamond Films and Devices

Chemistry, Electronics and Mechanics

Diamond Films and Devices

Chemistry, Electronics and Mechanics

Proefschrift

ter verkrijging van de graad van doctor
aan de Technische Universiteit Delft,
op gezag van de Rector Magnificus Prof. ir. K. C. A. M. Luyben,
voorzitter van het College voor Promoties,
in het openbaar te verdedigen op vrijdag 20 juni 2014 om 10:00 uur

door **Venkatesh SESHAN**
Master of Science in Nanoscale Science and Technology
Chalmers University of Technology, Sweden
geboren te Mannargudi, Tamil Nadu, India.

Dit proefschrift is goedgekeurd door de promotoren:

Prof. dr. E. J. R. Sudhölter

Prof. dr. ir. H. S. J. van der Zant

Copromotor: Dr. ir. L. C. P. M. de Smet

Samenstelling promotiecommissie:

Rector Magnificus	voorzitter
Prof. dr. E. J. R. Sudhölter	Technische Universiteit Delft, promotor
Prof. dr. ir. H. S. J. van der Zant	Technische Universiteit Delft, promotor
Dr. ir. L. C. P. M. de Smet	Technische Universiteit Delft, copromotor
Prof. dr. ir. R. Hanson	Technische Universiteit Delft
Prof. dr. R. J. Hamers	University of Wisconsin-Madison
Prof. dr. P. Wagner	Universiteit Hasselt
Prof. dr. S. G. Lemay	Universiteit Twente
Prof. dr. A. Schmidt-Ott	Technische Universiteit Delft, reservelid



Cover Design: BusyPencils (<http://busypencils.com>)

Copyright © 2014 V. Seshan

ISBN: 978-94-6186-320-1

All rights reserved. No part of this publication may be reproduced, stored in a retrieval system or transmitted in any form or by any means: electronic, mechanical, photocopying, recording or otherwise, without prior written permission of the author.

A free electronic version of this thesis can be downloaded from:

<http://www.library.tudelft.nl/dissertations>

Contents

1	Introduction	1
1.1	Diamond History	2
1.2	Synthetic Diamond: Towards Active Applications	3
1.3	Diamond and Chemistry	5
1.4	Diamond and Electronics	7
1.5	Diamond and Mechanics	8
1.6	Thesis Outline	9
	References	12
I	Chemistry Section	15
2	Hydrogen Termination of Diamond Films	17
2.1	Introduction	19
2.2	Experimental	20
2.3	Results and Discussion	24
2.4	Conclusion	34
	References	35
II	Electronics Section	39
3	Opto-electronic Properties of Diamond Films	41

3.1	Introduction	43
3.2	Experimental	44
3.3	Results and Discussion	48
3.4	Conclusion	58
	References	60
4	Electrical Characterization of Diamond Structures	63
4.1	Introduction	65
4.2	Experimental	66
4.3	Results and Discussion	68
4.4	Conclusion	75
	References	76
5	Nanogap Formation in Diamond Structures	79
5.1	Introduction	80
5.2	Experimental	81
5.3	Results and Discussion	82
5.4	Conclusion	89
	References	90
III	Mechanics Section	93
6	Fabrication and Characterization of Diamond Resonators	95
6.1	Introduction	97
6.2	Experimental	98
6.3	Results and Discussion	99
6.4	Conclusion	105
	References	106
	Appendix A: Supplementary Information Chapter 2	109
	Appendix B: Supplementary Information Chapter 5	117

Appendix C: Supplementary Information Chapter 6	119
Summary	121
Samenvatting	125
List of Publications	129
Acknowledgements	131

Chapter 1

Introduction

This chapter begins with a historic background on the origin of natural diamonds followed by scientific advancements in producing synthetic diamonds and their applications. In addition to the background information on diamond, a brief overview on the interesting chemical, electronic and mechanical properties of diamond is presented, which is also the motivation behind exploiting these properties for fundamental understanding and commercial applications as a part of this research work.

1.1 Diamond History

Among all the gemstones known to mankind, diamonds are treasured as rare and precious. For centuries diamonds have been part of human tradition and history.¹ It is often regarded as an emblem of status and affluence even today. The first exploration that led to the discovery of diamond was believed to be as early as 800 B.C. around Golconda in India.² However, the popularity of diamonds rose to prominence only in 1866 when a large diamond deposit in Kimberley, South Africa was uncovered. This led to influx of thousands of diamond explorers to the region, which later had profound influence on trade and development that changed the economic landscape of many southern countries in the African sub-continent.

In addition to its reputation as prized gemstone, diamond is also known for its exceptional material properties that are interesting to fundamental as well as applied sciences. Diamond is the hardest material found in nature, which is aptly reflected in its name.^{1,3} Diamond in ancient Greek is called *adamas* meaning unbreakable. This property makes diamond of great interest in many industrial, so-called passive applications mainly in the field of polishing and cutting tools. Other interesting properties of diamond are its optically transparency over a broad spectrum of wavelengths, extremely high heat conducting capacity at room temperature, biocompatibility and excellent electrical insulation and chemical inertness to aqueous environments.^{1,3} The combination of all these properties makes diamond a material of choice for additional high-technology engineering applications of which examples are given in the next paragraph. However, several factors such as its limited supply in nature, high cost and random shapes and sizes hinder full scale utilization of diamond material properties.

1.2 Synthetic Diamond: Towards Active Applications

The attractive properties of diamond inspired researchers to develop new ways to produce diamond material synthetically. The industrialized method to produce synthetic diamond makes use of high pressure and high temperature (HPHT), which was first marketed by General Electric.^{1,3,4} The HPHT technique replicates nature's way of forming diamond in which graphite is placed under high pressure and high temperature in the interior of the earth, resulting in the production of single crystals of diamond in the form of small grains. The diamond grains obtained from the HPHT technique are limited to cutting, grinding and machining mechanical components and polishing optics. The HPHT method is still popular for industrial applications as it allows mass production of high-quality diamond crystals at a low-cost.

The advancements of the chemical vapour deposition (CVD) technique enabled the production of diamond thin films.^{1,5} The CVD method offers a significant degree of control over the reproducibility of synthetic diamond in terms of quality and purity. This technique not only enabled full utilization of the superior properties of diamond, but it also led to renewed interest in diamond research in both academia and industry. Figure 1.1(a) shows a schematic of the most commonly used microwave plasma CVD reactor, which was also employed to produce the diamond films studied in this thesis. With this method the reproducibility of synthetic diamond in terms of quality and purity increased, facilitating industrial diamond applications.

The CVD technique uses diamond grains or powders as building blocks for growing diamond films. Prior to the CVD growth of a diamond film, a non-diamond substrate is pre-treated to enhance the nucleation of diamond grains. In the presence of precursor gases, i.e., a small fraction of carbon (typically < 5 %) in combination with a high amount of hydrogen gas, a tetrahedrally-bonded

carbon network is formed around the nucleation centres, which eventually grows into a diamond film. Unlike the HPHT technique, CVD processes do not require high pressures. Using the CVD technique, diamond films can be grown on flat as well as shaped substrates over a large area with properties that can be tuned according to the specification to suit high-technology engineering applications. For instance, free-standing diamond wafers and shaped diamond items such as speaker domes, precision optical components for high-power lasers, detector material for high-energy physics research and heat spreaders for the telecommunication industry are frequently produced using the CVD technique.^{3,5} Furthermore, the CVD diamond films have also been used for making diodes and field-effect transistors for high-power and high-frequency electronics and (bio)sensing applications.⁶

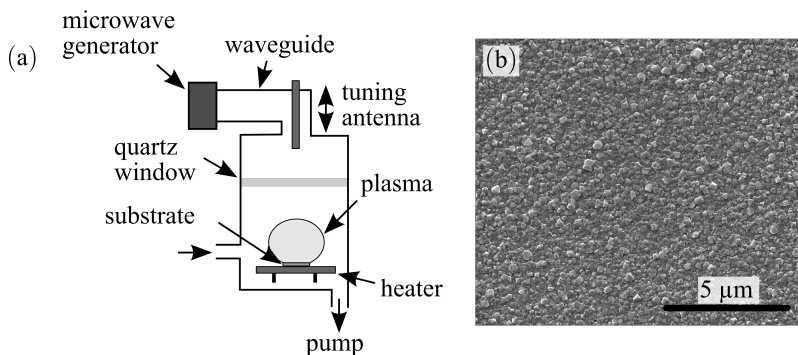


Figure 1.1: (a) Schematic representation of a microwave CVD plasma reactor adapted from reference 1 and (b) a scanning electron microscopy image showing the typical surface morphology of a nanocrystalline diamond film (courtesy of Dr. Stoffel Janssens, Hasselt University).

Diamond produced using the CVD technique can be classified as single crystalline or polycrystalline diamond. Single-crystalline diamond can only be grown homoepitaxially on a single-crystalline diamond substrate, whereas polycrystalline diamond is formed

when the CVD deposition process is carried out on a non-diamond substrate such as glass, silicon and quartz.⁵

One particular type of polycrystalline diamond that is typically grown using the CVD technique is nanocrystalline diamond (NCD).^{3,7} NCD films are made of diamond grains with typical sizes between 10 and 100 nm and a root mean square surface roughness of 10 to 30 nm. Figure 1.1(b) shows a scanning electron microscopy image of the surface morphology of a NCD film. By varying the growth conditions, NCD films can be grown with uniform grain size or in a columnar form; these films are referred to as 3D-NCD and 2D-NCD, respectively. While the preparation of single-crystalline diamond films is limited to substrate sizes on the cm scale, NCD films can be grown at a larger (wafer) scale.⁸ This enables the batch fabrication of devices on a single wafer making NCD films (economical and) appealing for fundamental and applied research. It is this aspect which formed the motivation behind using this material as a basis for my research.

The next three sections deal with a brief description of the properties of diamond material, which have been further studied in this thesis: the surface chemistry of diamond (Section 1.3), the (opto-)electronic properties of diamond films and devices (Section 1.4) and the mechanical properties of suspended diamond films (Section 1.5).

1.3 Diamond and Chemistry

For applications in (bio)sensors it is imperative for materials to be used as a substrate to display properties such as chemical stability in aqueous conditions and the possibility of covalent grafting of functional groups to its surface. The diamond obtained from the CVD growth process is typically hydrogen-terminated. Alternatively, diamond can be oxygen-terminated. Both forms of diamond are stable and there are different ways by which one can obtain a hydrogen or oxygen termination on diamond. For example,

hydrogen-terminated surfaces can be achieved by plasma techniques, hot-filament techniques or electrochemical means whereas oxygen termination of diamond can be obtained by contacting the diamond film with a boiling oxidizing acid, the use of an oxygen plasma, cathodic treatment or with ultraviolet/ozone methods.⁹⁻¹¹ The diamond surface can be modified from hydrogen to oxygen and vice versa. With the change in surface termination, the wettability of the diamond surface also changes. The hydrogen termination of diamond makes the surface hydrophobic whereas the oxygen termination makes it hydrophilic. In addition to the difference in wetting, interestingly the electron affinity of the surface also changes from a negative electron affinity for hydrogen-terminated surfaces to a positive electron affinity for oxygen-terminated surfaces.³ The main reason for the change in electron affinity is the difference in surface dipole between C–H and C–O bonds, which also influences the type of surface chemistry that can be performed on diamond films.

Interestingly, analogous to surfaces of silicon and germanium—two other group IV elements—hydrogen-terminated diamond can be modified via organic functionalization.¹² This can be carried out using photochemical, electrochemical or chemical methods.^{3,13,14} For instance, hydrogen-terminated diamond surfaces have been functionalized with alkenes, alkynes and diazonium salts. If functional groups like amines or carboxylic groups are present in the resulting layers it is possible to further functionalize the modified surface with a large variety of compounds, including DNA, enzymes and proteins. On the other hand, surface modification on oxygen-terminated diamond can be achieved only with chemical methods. Using this method, oxygen-terminated surfaces have been modified with silane molecules followed by the grafting of bio-molecules, presenting an alternative approach to achieve a bio-sensing platform. Diamond has been successfully utilized in implementing enzyme-modified amperometric sensors, enzyme-field effect transistors, DNA and protein sensors and potentiometric bio-sensors.^{3,15-17}

1.4 Diamond and Electronics

Diamond is a wide bandgap material (5.47 eV), which makes it a good insulator at room temperature.³ The electrical properties of diamond can be modified by doping with impurities or by exploiting surface-induced conductivity. Diamond can be made conducting by adding dopants such as boron, nitrogen and phosphorous atoms. Since boron atoms can be easily incorporated into the diamond crystal lattice during the CVD process, considerable research has been focused on manufacturing novel unipolar diamond devices using boron. The degree of doping plays an important role in determining the electrical properties of diamond. At low boron concentrations ($n_c < 10^{19} \text{ cm}^{-3}$), diamond shows extrinsic p-type semiconducting behaviour.¹⁸ When the boron doping concentration exceeds a critical value of $n_c \approx 2 \times 10^{20} \text{ cm}^{-3}$, diamond undergoes a doping-induced metal-to-insulator transition and conduction becomes metallic in nature. At low temperatures, the metallic films also exhibit superconductivity.¹⁹ The mobility values for boron-doped NCD are found to be between 0.2 to 1.8 $\text{cm}^2 \text{ V}^{-1}\text{s}^{-1}$.²⁰ The main reason for these rather low charge carrier mobilities is attributed to the presence of grain boundaries. Doped NCD films have been implemented as electron field emitters, electrochemical electrodes and even superconducting quantum interference devices (SQUIDs).^{3,21,22}

In addition to conductivity achieved through doping, diamond is known to show a unique p-type surface conductivity.^{3,23} This surface conduction phenomenon is based on a transfer doping mechanism on the hydrogen-terminated diamond. A diamond surface terminated with hydrogen leads to the formation of a two-dimensional hole channel several nanometers below the surface in the diamond layer. The main driver for this mechanism is believed to be atmospheric contamination, especially condensation of water vapour onto the hydrogenated diamond surface, which causes

electron transfer from the valence band of diamond to the surface layer containing ionized acceptors. The sheet conductance of hydrogen-terminated NCD is reported to be 10^{-4} to $10^{-5} \Omega^{-1}$ at room temperature and the surface density of hole charge carriers is between 10^{12} and 10^{13} cm^{-2} .³ For oxygen-terminated diamond, the change in surface termination from C–H to C–O bonds prevents the transfer doping mechanism to occur and hence no surface conductivity is observed. Surface conductivity has been explored for making field-effect transistors for sensing and device purposes.^{3,24-26}

1.5 Diamond and Mechanics

Apart from its chemical and electronic properties mentioned above, diamond has excellent mechanical properties. For instance, it has a low density ($\rho = 3500 \text{ kg.m}^{-3}$), a very low thermal expansion coefficient ($\alpha \approx 1.2 \text{ ppm.K}^{-1}$) and an extremely high Young's modulus ($E \approx 1100 \text{ GPa}$).^{3,7,27} Furthermore, doping in diamond allows integration of diamond material/devices into electronic circuits. These properties make diamond an ideal material for application in micro- and nano-electromechanical systems (MEMS and NEMS, respectively). Membranes of NCD films have been successfully applied to demonstrate nanomechanical resonators with frequencies up to 1.5 GHz and quality factors higher than 20,000.^{28,29} In addition, diamond materials in combination with silicon technologies have been used to produce complex MEMS and NEMS structures such as ring-resonator arrays, photonic crystals and micro-disks.³⁰⁻³² With the advancement in diamond processing technology, mechanical properties of NCD open new possibilities for interesting next generation NEMS applications such as nanophotonic circuits, ultra-sensitive force and mass transducers and bio-nanomechanical devices.³³⁻³⁵

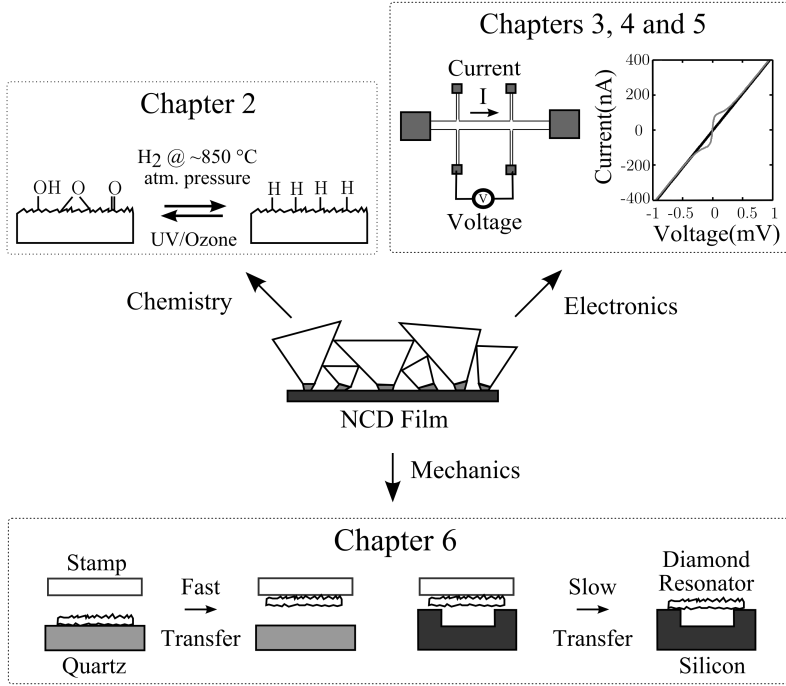
1.6 Thesis Outline

The goal of this thesis is to expand the fundamental understanding of the electronic properties of NCD films and as well as to increase their commercial applicability. Focus is given to the surface chemistry, to the electronic properties upon photoexcitation or the presence of a magnetic field and to the fabrication of nanogaps and mechanical resonators. Along these lines, the thesis is divided into three sections as shown in Scheme 1.1. The first section on chemistry deals with a new method to hydrogenate the surface of diamond (Chapter 2). The second section explores the (opto-) electronic transport properties for photovoltaics and molecular electronics applications (Chapters 3 - 5). The final section examines the mechanical properties of diamond resonators prepared by a novel stamping technique (Chapter 6).

Chapter 2 presents a new method to hydrogen terminate NCD films using molecular hydrogen at high-temperature and atmospheric pressure. The results obtained using the new method are compared in detail with those of the standard hydrogen plasma technique. It is shown that the new method yields results very similar to those of the standard hydrogen plasma technique. The presented atmospheric pressure technique could be easily scaled up to prepare hydrogenated diamond for industry in a cost-effective manner.

Chapter 3 describes an electrode-free way to study the optoelectronic properties such as the charge mobility and the carrier lifetime in NCD upon photoexcitation. The photoconductive properties of hydrogen and oxygen-terminated diamond are investigated for both undoped and doped NCD samples. The results can be understood using diamond band bending schemes based on the differences in surface termination and the presence of doping. In addition, the usefulness of the contactless time-resolved microwave

conductivity technique in studying the diamond photoconductive properties is introduced for the first time.



Scheme 1.1: Schematic overview of the thesis highlighting the three areas of study, i.e., the surface chemistry, the (opto-)electronics and the mechanics of NCD films and devices.

Chapter 4 deals with the fabrication and electrical characterization of conducting NCD Hall bar structures. The Hall bar structures are fabricated using standard lithography techniques. The electrical transport properties such as superconductivity, magneto-resistance and transverse resistance of these structures are measured at low temperature in the presence of a perpendicular magnetic field. The results presented in this chapter provide a starting point for more detailed studies on the superconducting properties of these films.

Chapter 5 introduces a unique current annealing technique to fabricate nanogaps and hybrid diamond/graphite nanostructures in doped NCD. The diamond structures are manufactured using lithographic techniques. Employing the current annealing technique, we demonstrate that electrodes with gaps as small as ~ 1 nm can be obtained. Furthermore, we report structural changes in the diamond due to the Joule heating during the current annealing process. This study presents a way to engineer diamond-based devices into hybrid diamond-graphitic structures with a possible use as nanoelectrodes in molecular electronics.

Chapter 6 demonstrates a proof-of-concept to fabricate diamond mechanical resonators by means of an innovative stamp-transfer technique. The resonators are characterized in an optical interferometer setup. We show that this stamping procedure is solvent-free and lithography-free, which makes it a low-cost and highly facile option for batch fabrication of NCD resonators.

References

- ¹ P. W. May, *Philos. Trans. R. Soc. Lond. Ser. A-Math. Phys. Eng. Sci.* **358**, 473-495 (2000).
- ² F. Ward, *National Geographic* **155**, 85-113 (1979).
- ³ R. S. Sussmann, *CVD Diamond for Electronic Devices and Sensors*. (Wiley Publications, West Sussex, UK, 2009).
- ⁴ J. E. Field, *The properties of natural and synthetic diamond*. (Academic Press London, 1992).
- ⁵ R. S. Balmer, J. R. Brandon, S. L. Clewes, H. K. Dhillon, J. M. Dodson, I. Friel, P. N. Inglis, T. D. Madgwick, M. L. Markham, T. P. Mollart, N. Perkins, G. A. Scarsbrook, D. J. Twitchen, A. J. Whitehead, J. J. Wilman, and S. M. Woollard, *J. Phys.-Condes. Matter* **21**, 364221 (2009).
- ⁶ C. J. H. Wort and R. S. Balmer, *Mater. Today* **11**, 22-28 (2008).
- ⁷ O. A. Williams, *Diamond Relat. Mater.* **20**, 621-640 (2011).
- ⁸ J. C. Zhang, J. W. Zimmer, R. T. Howe, and R. Maboudian, *Diamond Relat. Mater.* **17**, 23-28 (2008).
- ⁹ M. Wang, N. Simon, C. Decorse-Pascanut, M. Bouttemy, A. Etcheberry, M. S. Li, R. Boukherroub, and S. Szunerits, *Electrochim. Acta* **54**, 5818-5824 (2009).
- ¹⁰ Y. Mori, H. Kawarada, and A. Hiraki, *Appl. Phys. Lett.* **58**, 940-941 (1991).
- ¹¹ R. Hoffmann, A. Kriele, H. Obloh, J. Hees, M. Wolfer, W. Smirnov, N. Yang, and C. E. Nebel, *Appl. Phys. Lett.* **97**, 052103 (2010).
- ¹² S. F. Bent, *Surf. Sci.* **500**, 879-903 (2002).
- ¹³ C. E. Nebel, D. C. Shin, B. Rezek, N. Tokuda, H. Uetsuka, and H. Watanabe, *J. R. Soc. Interface* **4**, 439-461 (2007).
- ¹⁴ S. Szunerits and R. Boukherroub, *J. Solid State Electrochem.* **12**, 1205-1218 (2008).
- ¹⁵ H. Kawarada and A. R. Ruslinda, *Phys. Status Solidi A-Appl. Mat.* **208**, 2005-2016 (2011).

- ¹⁶ J. Rubio-Retama, J. Hernando, B. Lopez-Ruiz, A. Hartl, D. Steinmuller, M. Stutzmann, E. Lopez-Cabarcos, and J. A. Garrido, *Langmuir* **22**, 5837-5842 (2006).
- ¹⁷ Q. Wang, A. Kromka, J. Houdkova, O. Babchenko, B. Rezek, M. S. Li, R. Boukherroub, and S. Szunerits, *Langmuir* **28**, 587-592 (2012).
- ¹⁸ W. Gajewski, P. Achatz, O. A. Williams, K. Haenen, E. Bustarret, M. Stutzmann, and J. A. Garrido, *Physical Review B* **79**, (2009).
- ¹⁹ M. Nesladek, D. Tromson, C. Mer, P. Bergonzo, P. Hubik, and J. J. Mares, *Appl. Phys. Lett.* **88**, 232111 (2006).
- ²⁰ W. Gajewski, P. Achatz, O. A. Williams, K. Haenen, E. Bustarret, M. Stutzmann, and J. A. Garrido, *Phys. Rev. B* **79**, 045206 (2009).
- ²¹ E. Le Shim, M. H. Lee, M. Y. Lu, C. J. Kang, K. W. Lee, and Y. J. Choi, *J. Nanosci. Nanotechnol.* **12**, 8904-8907 (2012).
- ²² S. Mandal, T. Bautze, O. A. Williams, C. Naud, E. Bustarret, F. Omnes, P. Rodiere, T. Meunier, C. Bauerle, and L. Saminadayar, *ACS Nano* **5**, 7144-7148 (2011).
- ²³ C. E. Nebel, *Science* **318**, 1391-1392 (2007).
- ²⁴ H. Kozak, A. Kromka, O. Babchenko, and B. Rezek, *Sensor Letters* **8**, 482-487 (2010).
- ²⁵ W. S. Yang and R. J. Hamers, *Appl. Phys. Lett.* **85**, 3626-3628 (2004).
- ²⁶ A. Hartl, E. Schmich, J. A. Garrido, J. Hernando, S. C. R. Catharino, S. Walter, P. Feulner, A. Kromka, D. Steinmuller, and M. Stutzmann, *Nature Materials* **3**, 736-742 (2004).
- ²⁷ J. Philip, P. Hess, T. Feygelson, J. E. Butler, S. Chattopadhyay, K. H. Chen, and L. C. Chen, *J. Appl. Phys.* **93**, (2003).
- ²⁸ J. Wang, J. E. Butler, T. Feygelson, and C. T. C. Nguyen, in *IEEE International Conference on Micro Electro Mechanical Systems, Technical Digest* (IEEE, New York, 2004), pp. 641-644.

- ²⁹ A. Gaidarzhy, M. Imboden, P. Mohanty, J. Rankin, and B. W. Sheldon, *Appl. Phys. Lett.* **91**, 203503 (2007).
- ³⁰ J. W. Baldwin, M. K. Zalalutdinov, T. Feygelson, B. B. Pate, J. E. Butler, and B. H. Houston, *Diamond Relat. Mater.* **15**, 2061-2067 (2006).
- ³¹ C. F. Wang, R. Hanson, D. D. Awschalom, E. L. Hu, T. Feygelson, J. Yang, and J. E. Butler, *Appl. Phys. Lett.* **91**, 201112 (2007).
- ³² C. F. Wang, Y. S. Choi, J. C. Lee, E. L. Hu, J. Yang, and J. E. Butler, *Appl. Phys. Lett.* **90**, 081110 (2007).
- ³³ P. Rath, S. Khasminkaya, C. Nebel, C. Wild, and W. H. P. Pernice, *Nature Communications* **4**, 1690 (2013).
- ³⁴ A. Boisen, *Nat. Nanotechnol.* **4**, 404-405 (2009).
- ³⁵ J. P. Spatz, *Nature Materials* **4**, 115-116 (2005).

I

Chemistry Section

Chapter 2

Hydrogen Termination of Diamond Films

This chapter is based on the following publication:

- **V. Seshan**, D. Ullien, A. Castellanos-Gomez, S. Sachdeva, D. H. K. Murthy, T. J. Savenije, H. A. Ahmad, T. S. Nunney, S. D. Janssens, K. Haenen, M. Nesládek, H. S. J. van der Zant, E. J. R. Sudhölter, and L. C. P. M. de Smet “*Hydrogen termination of CVD diamond films by high-temperature annealing at atmospheric pressure*” The Journal of Chemical Physics, 2013 138(23): 234707.

A high-temperature procedure to hydrogenate diamond films using molecular hydrogen at atmospheric pressure was explored. Undoped and doped chemical vapour deposited (CVD) polycrystalline diamond films were treated according to our annealing method using a H₂ gas flow down to ~50 ml/min at ~850 °C. The films were extensively evaluated by surface wettability, electron affinity, elemental composition, photoconductivity and redox studies. In addition electrografting experiments were performed. The surface characteristics as well as the optoelectronic and redox properties of

the annealed films were found to be very similar to hydrogen plasma-treated films. Moreover, the presented method is compatible with atmospheric pressure and provides a low-cost solution to hydrogenate CVD diamond, which makes it interesting for industrial applications. The plausible mechanism for the hydrogen termination of CVD diamond films is based on the formation of surface carbon dangling bonds and carbon-carbon unsaturated bonds at the applied temperature, which react with molecular hydrogen to produce hydrogen-terminated surface.

2.1 Introduction

Diamond is an extraordinary material due to its distinctive bulk properties such as the highest thermal conductivity, extreme hardness, broad optical transparency, bio-compatibility, chemical inertness and excellent electrical insulation, which can be tailored to become semiconducting or normal conducting by doping with boron.^{1,2} As a result, diamond materials have been used in different applications ranging from micromechanical oscillators in acoustics to heat-sinks in radio frequency devices and also from coatings of cutting tools to transistors in electronic devices.^{1,2}

In addition to the above-mentioned superior bulk properties, the surface of diamond exhibits interesting properties too. For example, the type of surface termination affects the surface conductivity and electron affinity properties. In more detail, hydrogen-terminated diamond shows p-type surface conductivity with a negative electron affinity, whereas oxygen-terminated diamond shows surface insulating properties with a positive electron affinity.^{3,4} The change of surface termination of diamond (O-terminated vs. H-terminated) is reversible and controllable, which has created a niche market for diamond-based sensor devices that include biosensors, ion-sensitive field effect transistors and electrochemical sensors.¹ Oxygen termination of diamond can be done by contacting the diamond film with a boiling oxidizing acid, by oxygen plasma, by cathodic treatment or by ultraviolet (UV) /ozone treatment.^{5,6} Conversely, the hydrogen termination of diamond traditionally has been achieved using atomic hydrogen produced by either plasma or hot filament techniques.^{7,8} In spite of their popularity, these hydrogenation techniques are not widely available, but more importantly, they also have some drawbacks. Plasma techniques may cause undesired etching of the film, while hot filament techniques can sometimes cause surface contamination that originates from deposition of the filament material. Although hydrogen termination of diamond was recently achieved also

electrochemically, this method can be applied only to doped (i.e., conducting) diamond.⁹ As an alternative to the approaches mentioned above, hydrogenation using molecular hydrogen (H_2) has also been reported but only on undoped single crystal diamond (at ~ 800 °C and high vacuum conditions) and aggregated nano-diamond powder (at ~ 500 °C and low vacuum conditions).^{10,11} Nevertheless, the requirement of vacuum condition increases considerably the cost of the technique and constraints on the wafer sizes, hampering industrial application. Therefore, an alternative hydrogenation technique at atmospheric pressure would be highly attractive.

In this work, we show that high-temperature molecular hydrogen can also be applied to hydrogenate the surface of diamond films even at atmospheric pressure. The presented atmospheric pressure process, unlike high vacuum techniques, can be easily scaled up to fabricate cost-effective hydrogenated diamond for industry. The focus of this manuscript is on the demonstration of hydrogenation of both doped and undoped chemical vapour deposited (CVD) diamond films. CVD-prepared diamond films can be grown in a planar and non-planar form on different substrates, making it an interesting material for a wide variety of applications.² We extensively compared the results of our low-cost and highly facile method with the standard hydrogen plasma technique on the film properties by studying the wettability, electron affinity and elemental composition of the surface. In addition to surface properties, the optoelectronic and electrical properties of the surface-treated films were investigated.

2.2 Experimental

Two types of CVD diamond films were used for the experiments to show the versatility of the high-temperature annealing technique. The first type of samples used is undoped nanocrystalline diamond films (~ 150 nm thick with smaller grain size) grown on quartz at

Hasselt University. The CVD growth details of this film, including the measurement of the film thickness can be found elsewhere.¹² The second type of samples are doped electrochemical grade CVD diamond films (freestanding polycrystalline plates, 0.6 mm thick with larger grain size, resistivity: 0.02 - 0.18 Ohm.cm, boron doping $> 10^{20} \text{ cm}^{-3}$) that were purchased from Element 6 (UK). Each type of film was subjected to three different surface treatments, i.e., (1) UV/ozone treatment (UV/ozone-treated, used for reference purposes), (2) hydrogen-plasma treatment (H plasma-treated, used as a benchmark), and (3) high-temperature annealing treatment in molecular hydrogen gas at atmospheric pressure (H_2 -treated, the method presented here). In more detail, oxidation of the films was done under UV light in ambient condition for ~ 4 hours using a UV/Ozone ProCleaner system (BioForce Nanosciences Inc.). H plasma treatment of the films was carried out in a plasma reactor at $\sim 700 \text{ }^\circ\text{C}$ and 3500 W for 5 min. H_2 -treatment of the films was carried out in a non-plasma quartz tube reactor connected with a H_2 gas supply line. The films were heated to $\sim 850 \text{ }^\circ\text{C}$ under H_2 gas (99.999 % purity) flow. The films were kept for 20 min at $\sim 850 \text{ }^\circ\text{C}$ followed by cooling down to room temperature under a continuous H_2 gas flow. During the entire H_2 -treatment, the H_2 gas flow was typically maintained at $\sim 525 \text{ ml/min}$ under atmospheric pressure. Additionally, we found that the H_2 -treatment can also be carried out with a H_2 gas flow as low as $\sim 50 \text{ ml/min}$, a factor of 10 less than the previous flow rate, under atmospheric pressure. Notice that the results shown in the manuscript correspond to samples hydrogenated with a H_2 gas flow rate of $\sim 525 \text{ ml/min}$, but similar results were obtained for samples hydrogenated with $\sim 50 \text{ ml/min}$. All the films were UV/ozone-treated as an intermediate step before changing from H_2 -treatment to H plasma treatment and vice versa. This intermediate step was performed as a reset step to differentiate the results obtained from H_2 -treated and H plasma-treated film. To study the influence of above treatments on surface and

electronic properties, the films were subjected to different characterization techniques.

The surface wettability was studied with an Easy Drop goniometer (Krüss GmbH, Germany) at room temperature. Pictures of the droplets were taken immediately after dispensing 1 μl of MilliQ water on the sample and were subsequently analyzed using drop shape analysis software. The measurements were taken at 11 different spots on the film to obtain the average static water contact angle (WCA).

The difference in secondary electron emission of the surface was assessed using scanning electron microscopy (SEM, FEI Philips XL20). Before SEM analysis, the H_2 -treated film was partially covered with aluminum foil to protect it from oxidation while rest of the film was oxidized under UV light. After UV/ozone treatment, the foil was removed to obtain two different, well-separated areas with different surface terminations on the same film to study their secondary electron emission as reflected by the difference in relative contrast of the image.

The elemental analysis of CVD diamond surfaces that were exposed to ambient conditions up to several days was carried out using an X-ray Photoelectron Spectrometer (XPS, Thermo Fisher Scientific, K Alpha model). A monochromated Al K_α X-ray source was used. XPS measurements were taken in normal emission with a spot size of 400 μm at a base pressure of 10^{-9} mbar. During all XPS measurements the flood gun was enabled to compensate for the potential charging of surfaces. C 1s region scans were averaged over 10 scans and taken at 50 eV pass energy. The spectra were analyzed using Advantage processing software. The XPS spectra were background corrected using the “Smart” base line function available in the software, and peak fitting was done using a Gaussian (70%) - Lorentzian (30%) convolution function.

The electrical characterization of a undoped CVD film using a 2-probe technique was carried out to measure the surface resistance (see Appendix A, Section 1).

The optoelectronic properties of differently treated films were evaluated by measuring the photoconductivity using the electrodeless Time-Resolved Microwave Conductivity (TRMC) technique. Using this technique, the change in conductance of the film, on photo-excitation is recorded on tens of nanoseconds time scale without applying any external electrodes. A home-built TRMC set-up consists of an X-band (8.45 GHz) microwave cell. Diamond films were photo-excited with a 3 ns laser pulse from an optical parametric oscillator pumped by a Q-switched Nd:YAG laser (Vibrant II, Opotek). Photo-generation of mobile charge carriers in the film leads to an increase of the conductance, $\Delta G(t)$, and consequently to an enhanced absorption of microwave power by the sample. The time-dependent change of the conductance is obtained from the normalized change in microwave power ($\Delta P(t)/P$) reflected from the cell and is given by:

$$\Delta P(t)/P = -K\Delta G(t), \quad (2.1)$$

The geometrical dimensions of the cavity and dielectric properties of the media in the microwave cavity determine the sensitivity factor, K . The change in conductance is related to the number of photo-generated electrons and holes and the sum of their mobilities determined using the following equation: $\Delta G_{\max}/\beta e I_0 F_A$. Here, β is the ratio between the broad and narrow internal dimensions of the microwave cell, e is the electronic charge, I_0 is the incident light intensity and F_A is the fraction of incident light absorbed by the film. A detailed discussion related to this technique can be found elsewhere.^{13,14}

The redox properties of the doped films were measured using cyclic voltammetry (CV, Electrochemical analyzer/CH Instruments). For CV measurements, the diamond film was used as a working electrode with the current polarity setting as ‘cathodic positive’, a standard calomel electrode (SCE) as a reference electrode and a platinum wire as a counter electrode. The sample

was mounted in a Teflon cell with an O-ring of 0.25 cm² area, ensuring that the analysis areas for all electrochemical experiments were identical in size. The back contact was achieved via InGa eutectic. An electrolyte solution of 1M KNO₃ with 2mM Fe(CN)₆^{3-/4-} redox couple was used and the scan rate was 20 mV/s. Note that it has been reported that the electrochemical behavior of the Fe(CN)₆^{3-/4-} redox couple is very sensitive to the surface termination of the diamond electrode, making it an ideal redox couple for our study.¹⁵ To further study the reactivity of the H₂-treated diamond film, surface modification was performed using the electrochemical reduction of a diazonium salt. Dodecyldiazonium tetrafluoroborate was prepared by the standard method from the corresponding aniline with NaNO₂ in tetrafluoroboric acid.¹⁶ A solution of 2.5 mM dodecyldiazonium tetrafluoroborate in 25 mM of tetrabutylammonium tetrafluoroborate in acetonitrile was added to the cell and electrografting experiments were carried out at a scan rate 50 mV/sec. This experiment was also performed using an UV/ozone-treated diamond sample.

The undoped and doped films were characterized using WCA analysis, SEM, XPS and TRMC. In addition, the doped films were also characterized using CV.

2.3 Results and Discussion

In the first part of the results section data acquired from surface characterization techniques such as WCA, SEM and XPS are discussed to compare the results of different treatments on the surface of the film. For clarity, the WCA and SEM results of undoped samples are discussed here. The results obtained from the doped film were similar to those of the undoped films (see Appendix A, Section 2). The second part deals with the influence of surface treatment on the optoelectronic and redox properties of the film. The focus of the last part is on electrografting experiments.

The measurement of WCAs provides a quick and easy way to evaluate the relative hydrophilicity or hydrophobicity of surfaces. WCAs are of particular practical value in the case of switching from oxygen-terminated surfaces to hydrogen-terminated surfaces as these surfaces are hydrophilic and hydrophobic, respectively.^{17,18} Figures 2.1(a) and (b) show a drop of water on the UV/ozone-treated and the H₂-treated film, respectively. The WCA for the UV/ozone-treated CVD diamond film was found to be ~15°, while the WCA of the H₂-treated film was ~83°, which agrees well with the values obtained on H plasma-treated film (~84°) and reported values in the literature.^{19,20} These results show that the H plasma and H₂-treatment at atmospheric pressure produce surfaces with similar hydrophobicity.

Subsequently, CVD diamond films with different surface terminations were studied with SEM. It is known that in contrast to oxidized diamond surfaces—hydrogen-terminated diamond surfaces display strong electron emission.²¹ This difference has been attributed to the difference in electron affinity between H and O, which results in a lower energy barrier for electron emission in the case of hydrogen-terminated diamond surfaces. In a SEM image differences in secondary electron emission are reflected by the difference in contrast, which can also be used to discriminate between oxygen- and hydrogen-terminated domains of a diamond film.^{9,21} Figure 2.1(c) shows a SEM image of an H₂-treated sample that was partly covered during the oxidation process, resulting in a film with two different domains. In the SEM image, the part of the diamond film that was covered during the oxidation step is much brighter than the other (oxidized) part, suggesting the presence of hydrogen termination in the former case.^{9,21}

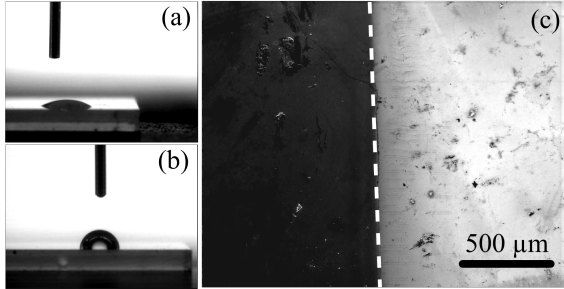


Figure 2.1: Water contact angle on (a) UV/ozone-treated and (b) H₂-treated undoped CVD diamond film. (c) SEM image of the undoped CVD diamond film showing two domains with a difference in contrast due to a difference in secondary electron emission. The dashed line (guide to the eye) indicates the boundary between the UV/ozone-treated and H₂-treated portion on the same film.

Although WCA and SEM studies provide a quick and macroscopic evaluation of relative surface properties, a more detailed analysis is needed to obtain insight into the type of functional groups on the diamond surface. To this end the samples were subsequently analysed with XPS, followed by a peak fitting procedure (Fig. 2.2). First, it is observed that the C 1s spectra of the H plasma-treated and H₂-treated diamond films are similar to each other, but different from the one of the UV/ozone-treated sample. In more detail, all spectra show peaks at ~ 284.0 and ~ 285.0 eV (peak I and II, respectively), which are indicative for photoelectrons from non-oxidized C 1s. As oxidized and hydrogenated CVD films are only different in terms of the interfacial atoms, most of the electrons probed by XPS are related to bulk C–C present in the top 5 to 10 nm. The difference in peak position of bulk C–C in the XPS spectra of oxidized and hydrogenated CVD films (~ 285.0 and ~ 284.0 eV, respectively) can be explained by the difference in band bending in these samples. It is known that the hydrogenated diamond film exhibits upward band bending caused by surface

Fermi level pinning.^{22,23} This reduces the energy barrier for electron emission from the bulk C–C groups detected by XPS. Hence, the dominant peak is observed at a lower binding energy (~ 284.0 eV) in Figs. 2.2(b) and (c). Upon oxidation, the Fermi level position at the diamond surface is modified leading to an increase in the energy barrier for electron emission and consequently shifting the bulk C–C peak to ~ 285.0 eV. This explanation suggests that the oxidized sample is not fully oxidized as Fig. 2.2(a) shows a peak at both positions. The contribution ~ 284.0 eV in Fig. 2.2(a) may originate from sub-surface areas that are not fully exposed to the ozone treatment and/or it may be related to surface roughness. Angle-resolved XPS may give more information on this issue. Also, the hydrogenated surfaces contain traces of oxidized carbon, but in those cases the peak I/peak II area ratio is comparable (28.4 and 25.5 for Fig. 2.2(b) and (c), respectively). The subpeaks at a binding energy > 285 eV (peak III, IV and V) can be assigned to photoelectrons from oxidized C 1s.^{9,23} Figure 2.2(a) shows subpeaks at 286.3 (peak III) and 288.1 eV (peak IV), which can be assigned to C–O and C=O, respectively.⁹ In the case of the hydrogenated samples only one subpeak related to oxidized C 1s is observed (peak V at ~ 286.8 eV, $< \sim 4$ % of all C 1s photoelectrons). The survey scans revealed the presence of oxygen (O 1s) and silicon (Si 1s) in all three cases, which we attribute to SiO₂ residues from the quartz tube reactor (see Appendix A, Section 3). However, the residue problem due to quartz tube could be overcome by using high-temperature, resistant alloy tube reactors.

In summary, the XPS analysis shows that the chemical composition of the hydrogenated diamond films is very similar.

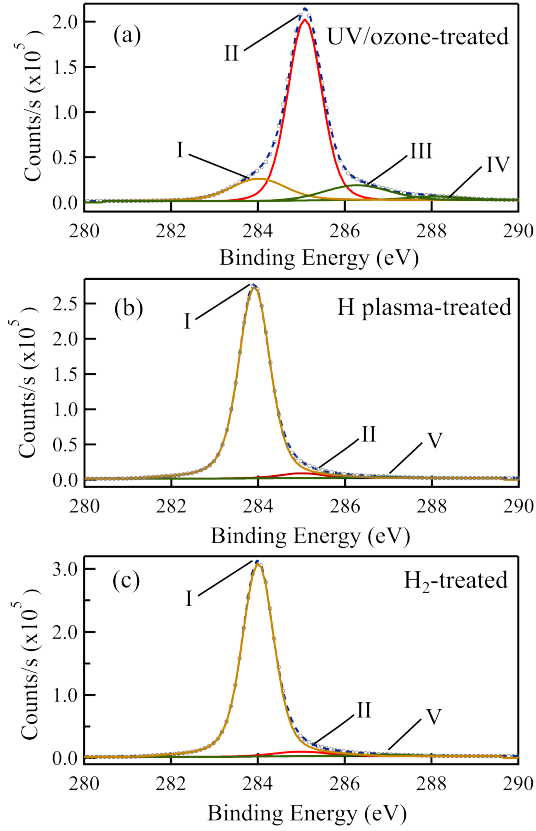


Figure 2.2: XPS C 1s region spectra of undoped CVD diamond films treated with (a) UV/ozone, (b) H plasma and (c) H₂-treatment at ~ 850 °C and atmospheric pressure. The dashed line represents the acquired spectrum; the convoluted peaks (solid lines, labeled as I, II, III, IV and V) were obtained via peak fitting. The total fit is given by circles. See main text for further details on the assignment.

The following section focuses on the effect of the surface treatment on the optoelectronic and electrical properties of CVD diamond films. To study the influence of surface treatment on the optoelectronic properties of the film, photoconductivity measurements were carried out using the electrodeless TRMC technique.

This technique has been used to study the charge transport properties, i.e., charge carrier mobility and charge carrier lifetime in semiconductor materials like silicon.^{13,24} Figure 2.3(a) shows the photoconductance transients obtained on pulsed excitation for the H plasma-treated (red curve) and H₂-treated (blue curve) film at 300 nm wavelength and 0.18 mJ/cm² incident intensity. Since the TRMC technique is electrodeless, the decay of the conductance is due to charge carrier recombination or trapping of mobile carriers. The intensity normalized photoconductance magnitudes, corresponding to $\Delta G_{\max}/\beta e I_0 F_A$, for H plasma-treated and H₂-treated diamond films were found to be similar and amount to ~ 0.06 cm²/Vs and ~ 0.09 cm²/Vs, respectively. Figure 2.3(b) shows the photoconductance transients normalized to unity for the H plasma-treated (red curve) and H₂-treated (blue curve) film on a shorter time scale. For both samples the half-lifetime ($\tau_{1/2}$) of the photo-generated charges was found to be ~ 225 ns as extracted from the decay of photoconductance transients. The similar decay kinetics suggests that both the charge carrier generation and recombination in the H₂-treated and H plasma-treated film follow the same photo-physical pathways. On the contrary, the $\tau_{1/2}$ of the photo-generated mobile charge carriers for UV/ozone-treated film is much shorter (~ 140 ps, insert in Fig. 2.3(a)) as deduced from the decay of photoconductance transient. The shorter $\tau_{1/2}$ could be attributed to the surface states introduced by oxygen termination in the bandgap region of the film leading to the trapping of mobile charges.^{25,26} It is important to note that these differences are only observed when using undoped diamond films (see Appendix A, Section 4) as the optoelectronic properties of doped films are dominated by bulk conduction.

To conclude this paragraph, the TRMC measurements show that also the opto-electronic properties of H₂-treated and H plasma-treated CVD diamond films are similar. A detailed investigation on the photoconductance mechanism in the hydrogen-

and oxygen-terminated diamond films using the TRMC technique is currently being carried out and will be addressed separately.

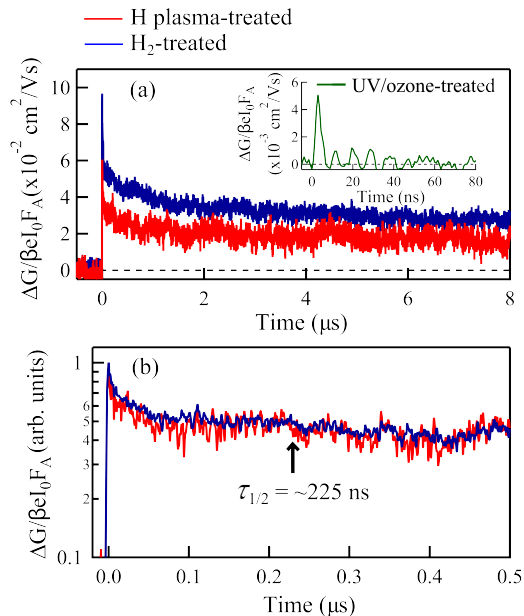


Figure 2.3: (a) Photoconductance transient for H plasma-treated (red curve) and H₂-treated (blue curve) undoped CVD diamond film measured using TRMC technique. The insert shows the photo-conductance transient of UV/ozone-treated (green curve) film. (b) Normalized photoconductance transient showing charge carrier lifetime data. The arrow indicates the half-lifetime ($\tau_{1/2}$).

To explore the effect of surface treatment on the electrochemical properties of the $\text{Fe}(\text{CN})_6^{3-/4-}$ redox analyte, doped CVD diamond films were used as a working electrode in CV measurements. Unlike TRMC, this technique requires the presence of dopants. Figure 2.4 shows cyclic voltammograms of an UV/ozone-treated (dashed curve), a H plasma-treated (dot-dashed curve), and a H₂-treated (solid curve) diamond films. The oxidation peak indicates oxidation of ferrocyanide ($\text{Fe}(\text{CN})_6^{4-}$) to ferricyanide ($\text{Fe}(\text{CN})_6^{3-}$) whereas the

reduction peak implies the reversed reaction (Fig. 2.4). The direction of the shift of the redox peak positions upon UV/ozone-treatment is in line with literature if one takes into account the difference in current polarization (in our case ‘cathodic positive’).^{9,15} The UV/ozone-treated and H₂-treated film show oxidative to reductive peak potential separation (ΔE_p) of 132 mV and 80 mV, respectively. The observation that H₂-treated films give a lower ΔE_p value in comparison to the UV/ozone-treated film is also in agreement with literature.^{9,15} The lower value of ΔE_p is an indication of a faster electron transfer process and more reversible behaviour.^{15,27} The difference in ΔE_p values related to the two different terminations has been attributed to the improved electronic interaction between the Fe(CN)₆^{3-/4-} redox couple and the hydrogen-terminated diamond surface.¹⁵ In addition, the H₂-treated film shows higher current peak values suggesting increased electrochemical activity unlike UV/ozone-treated film. The redox peaks of the H plasma-treated film overlap with those of H₂-treated film, suggesting a similar type of electron transfer kinetics for both systems. Finally, it is observed that the formal reduction potential (E^0) determined by $(E_p^{\text{ox}} + E_p^{\text{red}})/2$, is about 226 ± 1 mV in all three cases. The obtained E^0 value is in agreement with the reported values for ferro-/ferricyanide couple taking into account the type of reference electrode, concentration of potassium ions and nature of anions present.²⁸

The CV results clearly indicate a difference in the redox activity of UV/ozone-treated and H₂-treated/H plasma-treated film whereas an almost indistinguishable difference between H₂-treated and H plasma-treated film suggests similar type of surface termination.

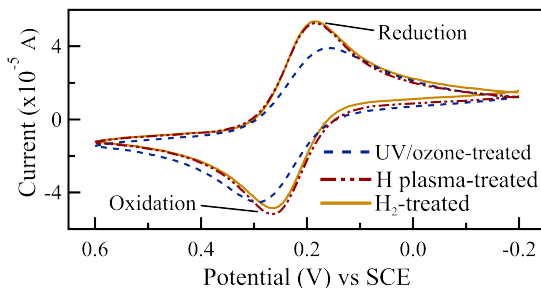


Figure 2.4: Cyclic voltammograms of UV/ozone-treated (dashed curve), H plasma-treated (dot-dashed curve) and H₂-treated (solid curve) doped CVD diamond film at a scan rate of 20 mV/sec. In all cases Fe(CN)₆^{3-/4-} was used as a redox couple.

Finally, the applicability of the H₂-treated film is shown by grafting it with aryl groups *via* the electrochemical reduction of a diazonium salt.²⁹⁻³¹ Figure 2.5(a) (solid line) shows the cyclic voltammogram of the electrochemical attachment of dodecylphenyl groups to the H₂-treated diamond surface. The peak at -0.56 V is attributed to the electroreduction. This value is higher than the reported value of the nitro-substituted phenyl diazonium salt,²⁹ which can be readily understood by difference in the electronegativity of the functional group: NO₂ is an electron withdrawing group, making it easier to electrograft as compared to an alkyl-substituted phenyl diazonium. As diazonium salts are reported to be reactive to OH-terminated diamond as well,²⁹ we also repeated our grafting experiment on UV/ozone-treated NCD as well (Fig. 2.5(a), dashed line). It is observed that the current amplitude of the latter plot is ~4 times as low as compared to the plot of the H₂-treated film, which is in line with the literature.²⁹ From Figures 2.5(b) and (c) it becomes clear that the redox activity of Fe(CN)₆^{3-/4-} is reduced for both electrografting experiments. These results show that diamond films treated with molecular hydrogen at high temperature and atmospheric con-

ditions can be derivatized electrochemically with organic functionalities.

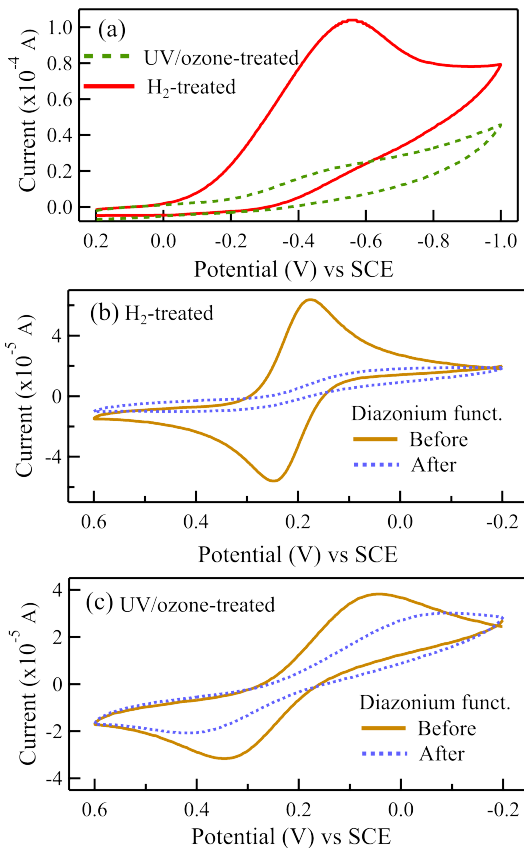


Figure 2.5: (a) Cyclic voltammogram of electrografting of 2.5 mM dodecyldiazonium tetrafluoroborate in acetonitrile on H₂-treated (solid line) and UV/ozone-treated (dashed line) doped CVD diamond film at a scan rate of 50 mV/sec. Cyclic voltammograms of (b) H₂-treated and (c) UV/ozone-treated doped CVD diamond film before (solid curve) and after (dotted curve) diazonium functionalization at a scan rate of 20 mV/sec. In the case of (b) and (c) Fe(CN)₆^{3-/4-} was used as a redox couple.

2.4 Conclusion

A high-temperature annealing procedure using molecular hydrogen at atmospheric pressure was explored as an alternative method to hydrogenate diamond films. Along with the surface properties also the optoelectronic and redox characteristics of the annealed films were found to be very similar to the properties of diamond films that were hydrogen plasma treated. The work indicates the presence of chemisorbed hydrogen atoms on the surface after the treatment with H_2 at ~ 850 °C and atmospheric pressure. As H_2 does not dissociate thermally at ~ 850 °C, the hydrogenation can be rationalized on the basis of the thermal dissociation of surface functional groups.^{32,33} This dissociation would subsequently result in the formation of active surface sites, like e.g. carbon dangling bonds and carbon-carbon unsaturated bonds.³⁴ These sites can then dissociate molecular hydrogen, leading to the formation of C–H bonds, analogous to what has been reported for the thermally induced hydrogenation of diamond powders.^{35,36} Further it has been shown that diazonium salts can be electrografted onto the H_2 -treated diamond films. The reference grafting experiment using a UV/ozone-treated diamond surface showed lower reduction amplitude, indicating that less molecules grafted onto this surface. Based on this difference we conclude that C–H bonds have been formed as hydrogenated diamond has proven to be more reactive towards the electrochemical grafting of diazonium salts as compared to oxidized diamond.²⁹

The presented hydrogenation method can be used for both undoped and doped CVD diamond and does not require high vacuum conditions, making it a cost-effective and an easily accessible alternative to hydrogenate diamond films.

References

- ¹ R. S. Sussmann, *CVD Diamond for Electronic Devices and Sensors*. (Wiley Publications, West Sussex, UK, 2009).
- ² R. S. Balmer, J. R. Brandon, S. L. Clewes, H. K. Dhillon, J. M. Dodson, I. Friel, P. N. Inglis, T. D. Madgwick, M. L. Markham, T. P. Mollart, N. Perkins, G. A. Scarsbrook, D. J. Twitchen, A. J. Whitehead, J. J. Wilman, and S. M. Woollard, *J. Phys.-Condes. Matter* **21**, 364221 (2009).
- ³ F. Maier, J. Ristein, and L. Ley, *Physical Review B* **64**, 165411 (2001).
- ⁴ F. Maier, M. Riedel, B. Mantel, J. Ristein, and L. Ley, *Phys. Rev. Lett.* **85**, 3472-3475 (2000).
- ⁵ M. Wang, N. Simon, C. Decorse-Pascanut, M. Bouttemy, A. Etcheberry, M. S. Li, R. Boukherroub, and S. Szunerits, *Electrochim. Acta* **54**, 5818-5824 (2009).
- ⁶ Y. Mori, H. Kawarada, and A. Hiraki, *Appl. Phys. Lett.* **58**, 940-941 (1991).
- ⁷ H. Kawarada, *Surf. Sci. Rep.* **26**, 205-259 (1996).
- ⁸ A. Lafosse, M. Bertin, S. Michaelson, R. Azria, R. Akhvlediani, and A. Hoffman, *Diamond Relat. Mater.* **17**, 949-953 (2008).
- ⁹ R. Hoffmann, A. Kriele, H. Obloh, J. Hees, M. Wolfer, W. Smirnov, N. Yang, and C. E. Nebel, *Appl. Phys. Lett.* **97**, 052103 (2010).
- ¹⁰ F. Fizzotti, A. Lo Giudice, C. Manfredotti, C. Manfredotti, M. Castellino, and E. Vittone, *Diamond Relat. Mater.* **16**, 836-839 (2007).
- ¹¹ O. A. Williams, J. Hees, C. Dieker, W. Jager, L. Kirste, and C. E. Nebel, *ACS Nano* **4**, 4824-4830 (2010).
- ¹² S. D. Janssens, S. Drijkoningen, M. Saitner, H. G. Boyen, P. Wagner, K. Larsson, and K. Haenen, *J. Chem. Phys.* **137**, 044702 (2012).

- ¹³ T. J. Savenije, P. van Veenendaal, M. P. de Haas, J. M. Warman, and R. E. I. Schropp, *J. Appl. Phys.* **91**, 5671-5676 (2002).
- ¹⁴ J. E. Kroeze, T. J. Savenije, M. J. W. Vermeulen, and J. M. Warman, *J. Phys. Chem. B* **107**, 7696-7705 (2003).
- ¹⁵ M. C. Granger and G. M. Swain, *J. Electrochem. Soc.* **146**, 4551-4558 (1999).
- ¹⁶ B. S. Furniss, A. J. Hannaford, V. Rogers, P. W. G. Smith, and A. R. Tatchell, *Vogel's Textbook of Practical Organic Chemistry, Including Qualitative Organic Analysis*, 4th ed. (Longman (London and New York), 1978), p.687.
- ¹⁷ Y. Kaibara, K. Sugata, M. Tachiki, H. Umezawa, and H. Kawarada, *Diamond Relat. Mater.* **12**, 560-564 (2003).
- ¹⁸ L. Ostrovskaya, V. Perevertailo, V. Ralchenko, A. Dementjev, and O. Loginova, *Diamond Relat. Mater.* **11**, 845-850 (2002).
- ¹⁹ M. Geisler and T. Hugel, *Adv. Mater.* **22**, 398-402 (2010).
- ²⁰ F. Pinzari, P. Ascarelli, E. Cappelli, G. Mattei, and R. Giorgi, *Diamond Relat. Mater.* **10**, 781-785 (2001).
- ²¹ J. B. Cui, J. Ristein, M. Stammer, K. Janischowsky, G. Kleber, and L. Ley, *Diamond Relat. Mater.* **9**, 1143-1147 (2000).
- ²² D. Ballutaud, N. Simon, H. Girard, E. Rzepka, and B. Bouchet-Fabre, *Diamond Relat. Mater.* **15**, 716-719 (2006).
- ²³ M. Wang, N. Simon, G. Charrier, M. Bouttemy, A. Etcheberry, M. S. Li, R. Boukherroub, and S. Szunerits, *Electrochem. Commun.* **12**, 351-354 (2010).
- ²⁴ C. Swiatkowski, A. Sanders, K. D. Buhre, and M. Kunst, *J. Appl. Phys.* **78**, 1763-1775 (1995).
- ²⁵ J. C. Zheng, X. N. Xie, A. T. S. Wee, and K. P. Loh, *Diamond Relat. Mater.* **10**, 500-505 (2001).
- ²⁶ W. Deferme, G. Tanasa, J. Amir, K. Haenen, M. Nesladek, and C. F. J. Flipse, *Diamond Relat. Mater.* **15**, 687-691 (2006).
- ²⁷ P. T. Kissinger and W. R. Heineman, *J. Chem. Educ.* **60**, 702-706 (1983).

- ²⁸ S. P. Rao, S. R. Singh, and S. R. Bandakavi, Proceedings of the Indian National Science Academy: Physical Sciences **44**, 333-335 (1978).
- ²⁹ N. J. Yang, J. H. Yu, H. Uetsuka, and C. E. Nebel, Electrochem. Commun. **11**, 2237-2240 (2009).
- ³⁰ H. Uetsuka, D. Shin, N. Tokuda, K. Saeki, and C. E. Nebel, Langmuir **23**, 3466-3472 (2007).
- ³¹ W. Jian, M. A. Firestone, O. Auciello, and J. A. Carlisle, Langmuir **20**, 11450-11456 (2004).
- ³² I. Langmuir, J. Am. Chem. Soc. **34**, 860-877 (1912).
- ³³ F. Jansen, I. Chen, and M. A. Machonkin, J. Appl. Phys. **66**, 5749-5755 (1989).
- ³⁴ A. C. Ferrari and J. Robertson, Physical Review B **64**, 075414 (2001).
- ³⁵ C. Manfredotti, P. Bonino, M. De La Pierre, E. Vittone, and C. Manfredotti, Diamond Relat. Mater. **19**, 279-283 (2010).
- ³⁶ T. Ando, M. Ishii, M. Kamo, and Y. Sato, J. Chem. Soc.-Faraday Trans. **89**, 1783-1789 (1993).

II

Electronics Section

Chapter 3

Opto-electronic Properties of Diamond Films

This chapter is based on the following work:

- **V. Seshan**, D. H. K. Murthy, A. Castellanos-Gomez, S. Sachdeva, H. A. Ahmad, S. D. Janssens, W. Janssen, K. Haenen, H. S. J. van der Zant, E. J. R. Sudhölter, T. J. Savenije, and L. C. P. M. de Smet “*Contactless photo-conductance study on undoped and doped nanocrystalline diamond films*” Submitted.

Hydrogen and oxygen surface-terminated nanocrystalline diamond (NCD) films are studied by the contactless time-resolved microwave conductivity (TRMC) technique and X-ray photoelectron spectroscopy (XPS). The opto-electronic properties of undoped NCD films are strongly affected by the type of surface termination. Upon changing the surface termination from oxygen to hydrogen, the TRMC signal rises dramatically. For an estimated quantum yield of 1 for sub-bandgap optical excitation the hole mobility of the hydrogen-terminated undoped NCD was found to be $\sim 0.27 \text{ cm}^2/\text{Vs}$

with a lifetime exceeding 1 μ s. Assuming a similar mobility for the oxygen-terminated undoped NCD a lifetime of ~ 100 ps was derived. Analysis of the valence band spectra obtained by XPS suggests that upon oxidation of undoped NCD the surface Fermi level shifts (towards an increased work function). This shift originates from the size and direction of the electronic dipole moment of the surface atoms, and leads to different types of band bending at the diamond/air interface in the presence of a water film. In the case of boron-doped NCD no shift of the work function is observed, which can be rationalized by pinning of the Fermi level. This is confirmed by TRMC results of boron-doped NCD, which show no dependency on the surface termination. We suggest that photo-excited electrons in boron-doped NCD occupy non-ionized boron dopants, leaving relatively long-lived mobile holes in the valence band.

3.1 Introduction

Since the last decade, the interest in diamond research, especially in nanocrystalline diamond (NCD) films, has grown significantly due to its unique material properties. NCD films exhibit high chemical stability in harsh environments, allow bio-chemical surface functionalization and can be doped with impurities to alter its electronic properties.^{1,2} Furthermore, NCD films can be fabricated on wafer-scale at low-cost using the chemical vapor deposition (CVD) technique. As a result, NCD films could be a solution to the growing need for an alternate electrode material in photovoltaic applications.^{3,4}

NCD films are made of crystalline diamond grains that are surrounded by non-diamond residual material such as sp^2 carbon phases and carbon with distorted sp^3 bonds and dangling bonds at the grain boundaries.⁵⁻⁷ Even though the diamond grains dominate the composition of the NCD films, the presence of defect states in the bulk of the material and also, defect states at the diamond surfaces affect the opto-electronic properties of the films.⁶⁻⁹ As a consequence, there is an increasing demand for a better understanding of the factors affecting the opto-electronic properties to further control and improve the film quality. Several studies on the defect distribution in the microcrystalline and NCD films using photocurrent measurements have been reported.¹⁰⁻¹³ In addition, the influence of experimental conditions such as ambient temperature, ultraviolet light irradiation and air pressure on photo-excited charge characteristics using photoluminescence techniques have also been discussed.¹⁴⁻¹⁶ Although photoluminescence techniques give important information on charge carrier dynamics of sub-bandgap states in NCD films, it is found to be less sensitive to the surface termination effect.¹⁷ Additionally, the surface properties of NCD films are significantly affected by hydrogen and oxygen termination in terms of surface wettability, electrical conductivity and electron affinity.^{18,19} Therefore, it is imperative to study the

effect of surface termination on the charge carrier kinetics and degree of Fermi level pinning using a complementary technique that can investigate surface sensitivity for better understanding of the fundamental charge generation and recombination processes in NCD films.

In the current article, the influence of the type of surface termination and boron and phosphorus doping, on the photoconductive properties of NCD films using the contactless time-resolved microwave conductivity (TRMC) technique are presented and discussed in detail. One very important characteristic of the TRMC technique is that no electrical contacts to the film are needed. As a result this approach overcomes contact problems that can be present in conventional photoconductivity measurements, including non-Ohmic contacts, contact resistance and adhesion problems. In addition to TRMC, valence band spectra of the NCD films are studied using X-ray photoelectron spectroscopy (XPS).

3.2 Experimental

Hereafter, we will refer to undoped NCD, boron-doped NCD and phosphorus-doped NCD films as U-NCD, B-NCD and P-NCD, respectively. All the NCD (undoped and doped) films were grown on quartz substrates under similar conditions. Prior to the CVD growth, the quartz substrates were seeded with diamond nanoparticles with a diameter of 7 - 10 nm.²⁰ The deposition of the NCD films was carried out using microwave plasma-enhanced CVD using standard H₂/CH₄ plasma. The reactor conditions for the film growth can be found in this work.²¹ The CVD deposition was stopped when the thickness reached ~150 nm based on the in-situ laser interferometer reading, which was followed by cooling down the films in the presence of a H₂ flow. This procedure yielded an undoped NCD film with hydrogen termination (U-NCD:H) on the surface. For the growth of B-NCD and P-NCD films, trimethylboron (boron concentration ~3000 ppm) and phosphine (phos-

phorus concentration $\sim 10,000$ ppm) gases were introduced, respectively, during the CVD process.

For photochemical oxidation, the as-grown NCD:H (undoped and doped) films were exposed to ultraviolet (UV) light under ambient conditions for ~ 4 hours using a UV/Ozone ProCleaner system (BioForce Nanosciences Inc.). This treatment resulted in NCD films with oxygen termination (NCD:O). Oxidized NCD films were re-hydrogenated using a non-plasma quartz tube reactor at ~ 850 °C for 20 min in the presence of H_2 gas, followed by gradual cooling to room temperature under a continuous H_2 flow to obtain NCD:H films. The details of hydrogen termination using H_2 gas can be found in this work.²² The cycle of re-oxidation and re-hydrogenation of NCD films was repeated at least 2 times to cross verify the characterization results obtained from the changes in film properties due to the change in surface termination. The hydrogenated and oxygenated NCD films were stored in air at room temperature.

The following part describes different characterization techniques performed on undoped and doped NCD films. The surface wettability of hydrogenated and oxygenated NCD films was studied using an Easy Drop goniometer (Krüss GmbH, Germany). A drop of 1 μ l MilliQ water was dispensed on the NCD film to examine the static water contact angle using drop-shape analysis software. To obtain an average water contact angle (WCA), measurements were performed at more than 5 different spots on the film.

To estimate the average (surface) grain size and the surface roughness of the NCD films, tapping-mode atomic force microscopy (AFM) was performed with a Nanoscope Dimension 3100 scanning probe microscope using silicon cantilevers (OLYMPUS) with a resonance frequency of ~ 350 kHz and a spring constant of ~ 26 N/m.

Raman spectroscopy was performed at 514 nm excitation wavelength with a laser spot size of ~ 400 nm using a Renishaw in via

micro-Raman spectrometer to identify the sp^3 bonding characteristics, i.e., the diamond phase of the NCD film.

The valence band measurements of NCD films were carried out using a monochromated Al K_α XPS (Thermo Fisher Scientific, K Alpha model). XPS measurements were performed at a base pressure of 10^{-7} mbar with a spot size of 400 μm . Valence band scans were taken at 100 eV pass energy at 3 different spots on the film with each scan averaged over 10 times. The flood gun was kept on during all XPS measurements to compensate for the potential charging of surfaces.

Optical transmission (I_T) and reflection (I_R) spectra of the NCD films were measured using a PERKIN ELMER Lambda 900 UV-Vis/NIR spectrometer. The spectra were used to obtain the fraction of incident photons absorbed (F_A) by the film, which is given by:

$$F_A = 1 - (I_T + I_R)/I_0, \quad (3.1)$$

where I_0 is the incident light intensity.

Photoconductance measurements on the NCD films were carried out using the TRMC technique at room temperature and ambient pressure. Previously, this technique has been used to study the charge transport properties in a wide range of materials including organic blend films and (nanostructured) inorganic semiconductors.²³⁻²⁵ In one of our recent studies, we used the TRMC technique for the first time to study diamond films in an electrode-free way.²² A new method to hydrogenate CVD diamond films by high-temperature annealing at atmospheric pressure was introduced. To compare the resulting films with films that were hydrogenated with the established plasma-based method, a variety of techniques was used, including TRMC. A detailed description on the TRMC technique can be found in this review.²⁵ Briefly, the home-built TRMC setup consists of an X-band (8.4 GHz) microwave cell (Fig. 3.1). The NCD film was photo-excited with a 3 ns laser pulse from

an optical parametric oscillator pumped by a Q-switched Nd:YAG laser (Vibrant II, Opotek). The overall response time of the setup including the electronics used for detection is ~ 1 ns. The measurements were performed at 300 nm (4.13 eV), 580 nm (2.14 eV) and 700 nm (1.77 eV) wavelengths, which all correspond to energies smaller than bandgap of diamond.

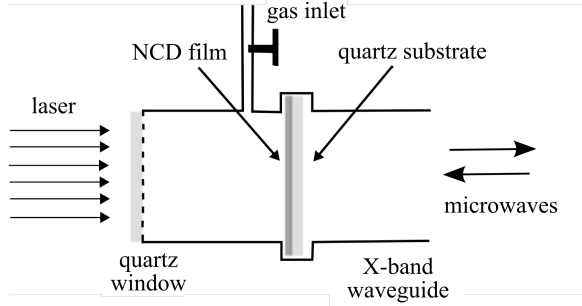


Figure 3.1: Schematic of the microwave cell used in the TRMC technique.

Photo-excitation of the NCD film results in the generation of mobile charge carriers in the film, which consequently changes the conductance (ΔG) of the film. Since there is no external electrode/contact to the film, the photo-generated mobile charges eventually decay with time via recombination and/or trapping. The change in conductance within the film ($\Delta G(t)$) can be related to the normalized change in the reflected power ($\Delta P(t)/P$) from the microwave cell and is given by:²⁵

$$\Delta P(t)/P = -K\Delta G(t), \quad (3.2)$$

where K represents a sensitivity factor that is determined from the dimensions of the microwave cell and the geometrical properties of the media in the microwave cell. The time-dependent change in conductance ($\Delta G(t)$) can be further expressed in terms of the number of photo-induced electrons and holes and the sum of their mobilities. If the decay of the photo-induced charges is longer than

the time resolution of the detection system, then the maximum change in conductance (ΔG_{\max}) with respect to the incident light gives the following equation:

$$\Phi\Sigma\mu = \Delta G_{\max}/\beta e I_0 F_A, \quad (3.3)$$

Here, $\Phi\Sigma\mu$ denotes the product of the quantum yield of the photo-induced charges (Φ) per absorbed photon and the sum of electrons and holes mobilities ($\Sigma\mu$), I_0 is the incident light intensity per pulse and F_A is the fraction of incident photon absorbed. β is the ratio between the broad and narrow internal dimensions of the microwave cell and e is the electron charge.

3.3 Results and Discussion

In the first part of this section, we elaborate on the film characterization, which includes WCA for surface wettability, AFM for surface topography and grain size, Raman spectroscopy for the presence of crystalline diamond phase and XPS measurements for valence band profile. The second part focuses on the TRMC photo-conductance data of hydrogen and oxygen-terminated NCD undoped, boron-doped and phosphorus-doped.

To evaluate the surface wetting properties, WCA measurements were carried out. For boron-doped, phosphorus-doped and undoped NCD:O films, the average static water contact angle was found to be less than 20° while values of 80° to 90° were found for the corresponding NCD:H films, which is in line with reported values.²⁶

For characterizing the topography and the surface grain size of the NCD surface, AFM was performed. Figure 3.2 depicts an AFM topography image of an undoped NCD:O film showing the nanocrystalline character of the film with a high density of grains. The average surface grain size of the film was found to be 60 ± 10 nm and the root mean square value of the surface roughness is found to be ~ 17 nm.

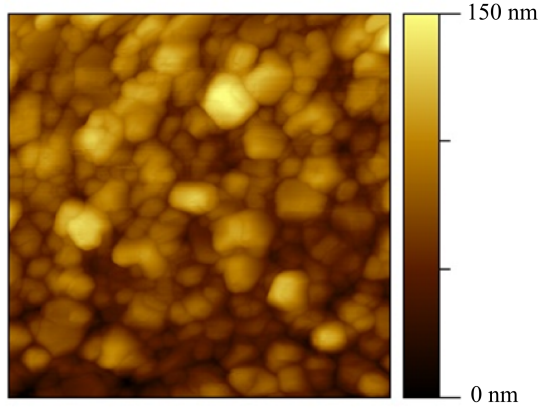


Figure 3.2: An AFM topography image ($2\ \mu\text{m} \times 2\ \mu\text{m}$) of an undoped NCD:O film.

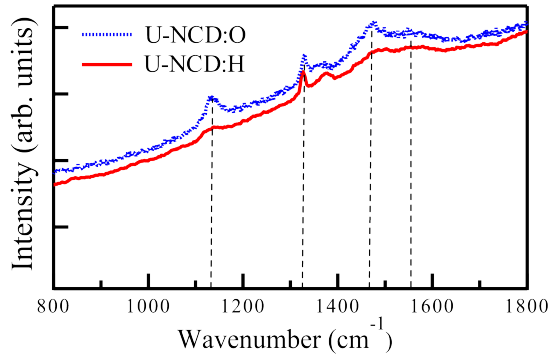


Figure 3.3: Raman spectra of U-NCD:O and U-NCD:H films.

In order to identify sp^3 phase in the undoped NCD:H and NCD:O films, Raman spectroscopy was carried out. Figure 3.3 represents the Raman spectra of U-NCD:O and U-NCD:H films with a similar peak at $1329\ \text{cm}^{-1}$ that corresponds to the sp^3 vibrational mode of diamond.²⁷ The broadening and shifting of the diamond peak from the characteristic $1332\ \text{cm}^{-1}$ line can be associated with

grain size of the NCD film and the eventual presence of strain.²⁷ The peaks observed at 1135 cm^{-1} and 1475 cm^{-1} correspond to the C–H vibration modes, which also have been reported previously in these kind of films.²⁸ The broad hump around at 1550 cm^{-1} is attributed to sp^2 -bonded carbon, which is predominantly expected to be present at the grain boundaries.²⁹

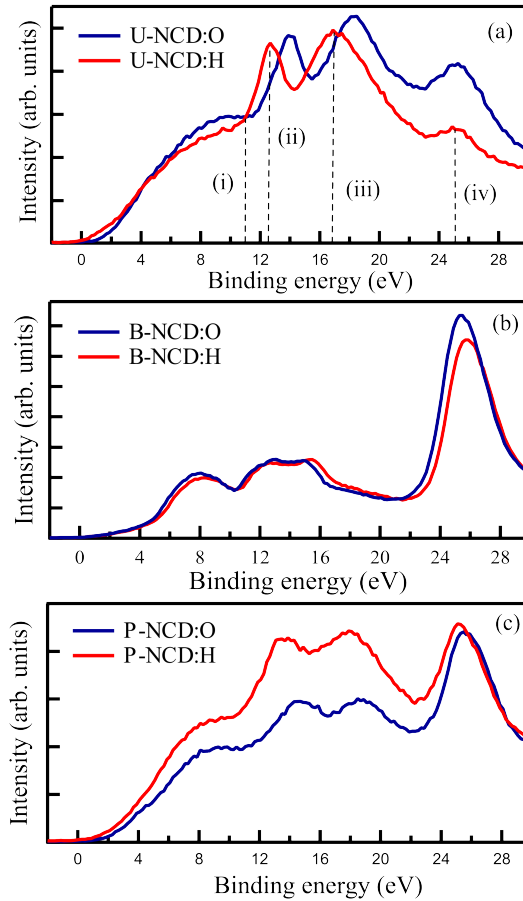


Figure 3.4: XPS valence band spectra of (a) U-NCD, (b) B-NCD and (c) P-NCD films.

To further characterize the surface of NCD films, XPS valence band measurements were carried out. Figure 3.4 shows XPS valence band spectra for undoped and doped NCD films. The U-NCD:H plot consists of 4 features as identified by reference 30 (Fig. 3.4(a), dashed lines): (i) a peak below ~ 11 eV is attributed to the valence bands related to the C 2p levels, which are linked to H 1s orbitals, (ii) a peak around ~ 12 eV that corresponds to the valence band derived from the 2s–2p hybridized levels of the diamond, (iii) a peak around ~ 17 eV related to the 2s level of the diamond and (iv) a low-intensity peak around ~ 25 eV, which is ascribed to the photoemission from O 2s.³⁰ In comparison to the U-NCD:H film, the C-related peaks (i.e., peaks i-iii) in the valence band spectrum of U-NCD:O film are shifted towards higher binding energies. This shift can be attributed to the surface dipoles increasing the work function, which is consistent with the shift observed for C 1s core-level spectra in the U-NCD:O film.^{22,30} In addition, the photo-emission peak due to O 2s (peak iv) is higher in intensity for the U-NCD:O film compared to the U-NCD:H film. This difference is in agreement with the higher O 1s/C 1s atomic concentration ratio in U-NCD:O film.²² Interestingly, for B-NCD:H and B-NCD:O films (Fig. 3.4(b)), there is hardly any shift observed in the valence band binding energies. This could be due to high boron doping in our film (boron concentration ~ 3000 ppm, bulk concentration of boron $\approx 1.6 \times 10^{21}$ cm⁻³), which pins the Fermi level at the boron level near the valence band.³¹ The O 2s photoemission peak in B-NCD:H is found to be slightly lower in intensity as compared to B-NCD:O, which is not significant as compared to the differences observed in U-NCD films. However, the WCA measurements of B-NCD:H and B-NCD:O surfaces showed a clear difference in surface wettability indicating different surface termination. The valence band data of the P-NCD films is given in Fig. 3.4(c) and clearly shows that the Fermi level pinning is less dominant as compared to the B-NCD films.

To conclude from the first part of the results and discussion, the difference in the valence band spectra of U-NCD:H and U-NCD:O films is in line with the difference in the related band bending profiles, due to a shift in the Fermi level. On the contrary, the valence band spectra of the B-NCD:H and B-NCD:O films were found to be very similar, which can be understood by pinning of the Fermi level at the surface.

Table 3.1: Summary of the $\Phi\Sigma\mu$ and lifetime values for the hydrogen- and oxygen-terminated undoped, boron-doped and phosphorus-doped NCD films.

Surface Film	Hydrogen-terminated			Oxygen-terminated		
	$\Phi\Sigma\mu$	Lifetime		$\Phi\Sigma\mu$	Lifetime	
U-NCD	~ 0.27 cm^2/Vs	~ 1 μs (τ_1)	~ 10 μs (τ_2)	~ 0.005 cm^2/Vs	~ 100 ps (τ)	
B-NCD	~ 0.040 cm^2/Vs	~ 120 ns (τ_1)	~ 1.91 μs (τ_2)	~ 0.057 cm^2/Vs	~ 108 ns (τ_1)	~ 1.78 μs (τ_2)
P-NCD	~ 0.0023 cm^2/Vs	— ^a		— ^a	— ^a	

^a the signal-to-noise ratio of the TRMC signal was found to be too low to determine this value.

Next, the samples were studied with TRMC. Figure 3.5(a) shows a TRMC trace obtained on the excitation of U-NCD:H by a nanosecond laser pulse of 300 nm. From the trace two characteristic parameters can be extracted: the magnitude given by the maximum value of $\Delta G/\beta e I_0 F_A$ indicated by the arrow in Fig. 3.5(a), and secondly the decay time. According to Equation 3.3, the value of $\Delta G/\beta e I_0 F_A$ corresponds to the product of the quantum yield of photo-induced charges (Φ) per absorbed photon and the sum of electron and hole mobilities ($\Sigma\mu$). Assuming a quantum yield of 1, a lower limit of ~ 0.27 cm^2/Vs for the sum mobility of the photo-generated charges is deduced. For U-NCD:H mobility

values up to $1 \text{ cm}^2/\text{Vs}$ have been reported agreeing approximately with the values found in this work.³² The inset of Fig. 3.5(a) shows the life-time (dotted line) of the photo-generated charge carriers and the resulting fit (solid line) using a double exponential function, yielding lifetimes of $\sim 1 \text{ } \mu\text{s}$ (τ_1) and $\sim 10 \text{ } \mu\text{s}$ (τ_2) (Table 3.1).

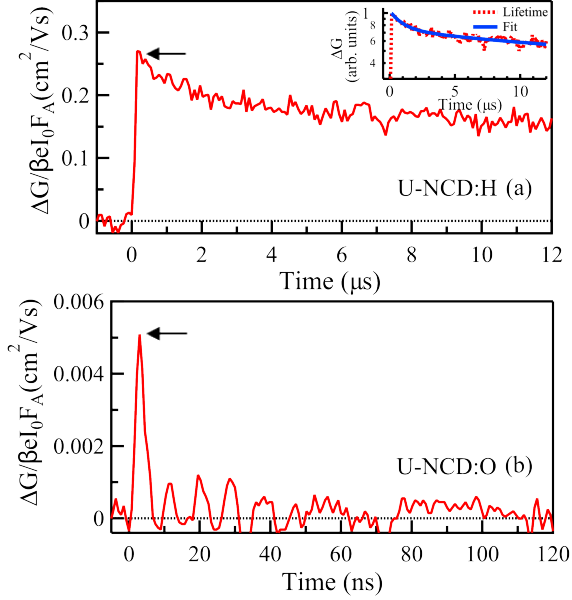


Figure 3.5: Photoconductance transient at 300 nm wavelength of the U-NCD:H film plotted in two ways: (a) linear axes, showing the maximum value of $\Delta G/\beta e I_0 F_A$, indicated by the arrow and (inset) log-lin plot showing the charge carrier lifetime data (dotted line) and corresponding fit using a double exponential function (solid line). (b) Photoconductance transient of U-NCD:O at 300 nm wavelength. The arrow indicates the maximum value of the photoconductance magnitude.

For U-NCD:O (Fig. 3.5(b)) the TRMC trace reaches a maximum value of only $\sim 0.005 \text{ cm}^2/\text{Vs}$, which is more than one order of the magnitude smaller than the value of U-NCD:H (Table 3.1). The trace resembles the shape of the laser pulse, indicating the

lifetime of the photo-induced charges is less than a few nanoseconds, i.e., much shorter than that of U-NCD:H. To estimate the charge carrier lifetime, the obtained transient is deconvoluted assuming a first order decay (τ) and a mobility value of $\sim 0.27 \text{ cm}^2/\text{Vs}$ yielding a τ of ~ 100 picoseconds.²⁴

To study the influence of the charge carrier density on the photoconductance properties of U-NCD:H, TRMC experiments are performed at various incident intensities and wavelengths. Figure 3.6 (white section, top) shows the maximum values of the photoconductance expressed in $\Phi\Sigma\mu$ as a function of the laser pulse intensity (I_0) at three different sub-bandgap wavelengths, i.e., 300 nm, 580 nm and 700 nm. At $I_0 > 2 \times 10^{13}$ photons/cm² the value of $\Phi\Sigma\mu$ decreases with increasing intensity. This could be due to second order recombination reducing the number of photo-induced mobile charges or due to charge carrier scattering resulting in a lowering of the mobility.³³ Interestingly, the dependence of the $\Phi\Sigma\mu$ values on I_0 is the same for all measured wavelengths. These results suggest that for U-NCD:H the charge carrier generation and recombination kinetics are identical for all three photon energies.

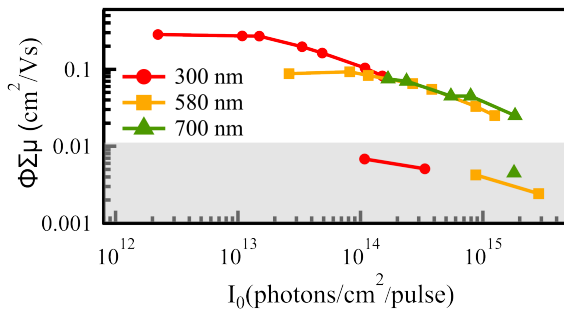


Figure 3.6: Photoconductance magnitude ($\Phi\Sigma\mu$) values as a function of intensity (I_0) for U-NCD:H (white section, top) and U-NCD:O (grey section, bottom) at different excitation wavelengths.

Figure 3.6 (grey section, bottom) includes the maximum values of $\Phi\Sigma\mu$ for U-NCD:O as a function of I_0 at the same three wave-

lengths. Only at intensities above 10^{14} photons/cm², a small photo-conductance signal could be observed. For intensities lower than 10^{14} photons/cm² the signal to noise ratio was too small to be resolved.

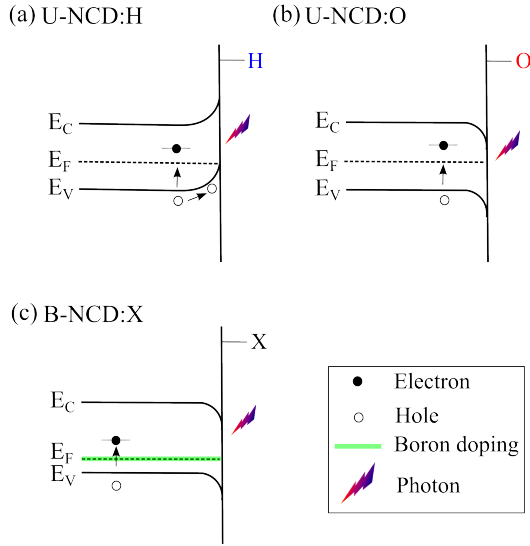


Figure 3.7: Qualitative band bending profiles for (a) U-NCD:H, (b) U-NCD:O and (c) B-NCD:X (X implies H or O). The arrows indicate the formation of electron-hole pair on photo-excitation. E_F , E_C and E_V are the position of Fermi level, conduction band minimum and valence band maximum, respectively. The bandgap states between E_V and E_F act as hole traps whereas bandgap states between E_F and E_C act as electron traps. The legend is given in the box on the bottom left side of the figure.

Since an electronic transition from the valence band to the conduction band of diamond requires an energy of ≥ 5.47 eV (~ 226 nm) all photon energies used in this work result in an electronic transition to or from an intra-bandgap state; most likely an electron from the valence band to an empty π^* state. The differences observed in the TRMC results obtained for U-NCD:H and U-NCD:O can be rationalized by a change in the band bending

diagram at the interface with air, due to the differences in surface termination. It has been reported previously that the electric dipoles caused by hydrogen atoms at the surface of diamond, lead to a reduction of the surface Fermi level (towards a decreased work function). This results in an upward band bending diagram in the presence of a water film at the diamond/air interface, facilitating the dissociation of an electron-hole pair formed on photo-excitation.³⁴⁻³⁶ We postulate that upon sub-bandgap excitation of U-NCD:H electrons are trapped in empty π^* states leaving behind mobile holes in the valence band (Fig. 3.7(a)), which are drifted towards the surface. This suggests that the obtained mobility value of $\sim 0.27 \text{ cm}^2/\text{Vs}$ from the TRMC measurements is due to mobile holes, comparable to the hole mobility reported for both boron-doped and undoped hydrogenated NCD films.^{8,21,32} In the case of U-NCD:O, oxygen termination results in a downward band bending diagram due to the opposite electric dipole moment of oxygen as compared to hydrogen termination (Fig. 3.7(b)).^{36,37} Photo-excited electrons residing in π^* states are immobile, while the corresponding holes remain in the bulk of the grains of the NCD. Hence, fast second order electron-hole recombination can take place explaining the rapid TRMC decay of ~ 100 picoseconds. The band-bending diagram presented here to explain the TRMC results agrees well with the XPS valence band measurements on U-NCD:H and U-NCD:O (Fig. 3.4(a)) discussed above, which show a shift in the surface Fermi levels.

To study the effect of doping on the opto-electronic properties of NCD, TRMC measurements were performed on boron (B-NCD) and phosphorous (P-NCD) doped films. Figure 3.8(a) shows the TRMC traces of hydrogen (B-NCD:H) and oxygen (B-NCD:O) terminated NCD, which interestingly are found to be similar. If Φ is assumed to be 1, the lower limit of the mobility is $\sim 0.05 \text{ cm}^2/\text{Vs}$. Note that although a high boron concentration is used (boron concentration $\sim 3000 \text{ ppm}$, bulk concentration of boron $\approx 1.6 \times 10^{21} \text{ cm}^{-3}$) the majority of dopants are not ionized. According to Baker

et al. the high dopant concentration in crystalline diamond leads to Fermi level pinning near the valence band edge (Fig. 3.7(c)).³¹ Hence, it is expected that the surface dipole moments of the terminal groups do not affect the Fermi level. Thus for boron doped, hydrogen- or oxygen-terminated NCD the band diagrams are equal, which explains the similar TRMC traces. In ambient conditions, a thin depletion layer is expected with a downward band bending as shown in Fig. 3.7(c).³⁸ We suggest that on photo-excitation electrons are promoted to an empty π^* state. From there the electrons could occupy a non-ionized boron dopant, leaving a relatively long-lived mobile hole in the valence band (Table 3.1 for B-NCD lifetime values). This interpretation is in accordance with electrical conductivity measurements on highly doped, single-crystalline diamond films.³¹ The present measurements demonstrate that also for NCD films doping leads to Fermi level pinning. Moreover, this model is in line with our interpretation of the XPS valence band measurements for B-NCD:H and B-NCD:O (Fig. 3.4(b)) discussed above.

Figure 3.8(b) shows a TRMC trace of a P-NCD:H film, which reaches a maximum value of $\sim 0.0023 \text{ cm}^2/\text{Vs}$ and decays within a few nanoseconds. For P-NCD:O no detectable TRMC signal could be collected (data not shown). Clearly, the type of doping hugely affects the yield and lifetime of photo-generated charges. Phosphorous doping leads to a shift of the Fermi level towards the conduction band minimum.³⁹ There is not much literature on P-NCD films⁴⁰ and to our knowledge it is not exactly known to what extent phosphorus doping leads to mobile electrons. Therefore, the position of the Fermi level is not clear disabling picturing a band diagram. However, we suggest that optical excitation leads to population of an empty π^* state. In contrast to boron doping, electrons cannot be captured and will recombine rapidly explaining the very short lifetimes observed in the TRMC traces.

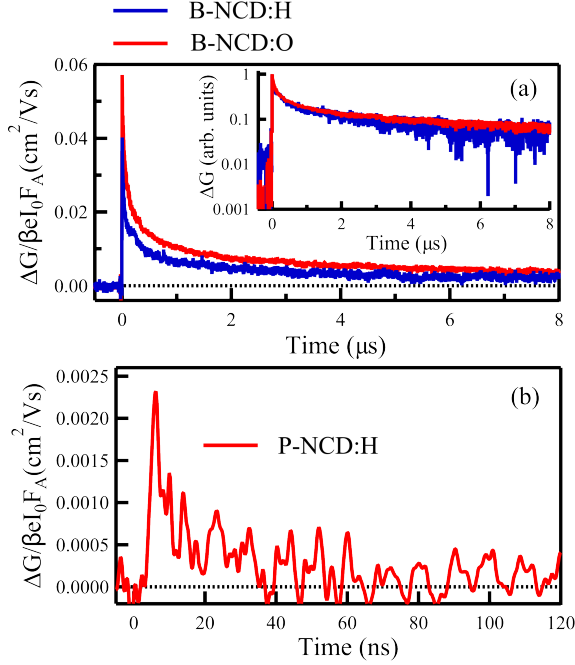


Figure 3.8: Photoconductance transients of (a) B-NCD and (b) P-NCD at 300 nm wavelength. Note the different time scales. The inset in (a) shows the charge carrier lifetime data for the B-NCD film.

3.4 Conclusion

The contactless TRMC technique along with the X-ray photoelectron spectroscopy has been used to study the effect of hydrogen and oxygen termination on the surface Fermi levels and the photoconductive properties of undoped and doped NCD films. The photoconductance signal and the charge carrier lifetimes are significantly affected by the type of surface termination on the undoped NCD films, whereas no surface termination effect was observed for boron-doped films. These results are explained on the basis of the differences in the band bending diagrams at the diamond surfaces. The photoconductance results from the TRMC technique provide a direct quantification of the charge carrier

mobility and its decay dynamics without problems related to electrode contact issues. Furthermore, the charge transport study presented here provides valuable information to investigate the effect of surface functionalization on NCD films for potential surface-based (opto-)electronic sensor applications and the charge transfer between diamond-organic systems for solar cell applications.⁴¹

References

- ¹ R. S. Sussmann, *CVD Diamond for Electronic Devices and Sensors*. (Wiley Publications, West Sussex, UK, 2009).
- ² C. E. Nebel, D. Shin, B. Rezek, N. Tokuda, H. Uetsuka, and H. Watanabe, *J. R. Soc. Interface* **4**, 439-461 (2007).
- ³ H. M. Hubbard, *Science* **244**, 297-304 (1989).
- ⁴ C. H. Y. X. Lim, Y. L. Zhong, S. Janssens, M. Nesladek, and K. P. Loh, *Adv. Funct. Mater.* **20**, 1313-1318 (2010).
- ⁵ O. A. Williams, *Diamond Relat. Mater.* **20**, 621-640 (2011).
- ⁶ O. A. Williams, M. Nesladek, M. Daenen, S. Michaelson, A. Hoffman, E. Osawa, K. Haenen, and R. B. Jackman, *Diamond Relat. Mater.* **17**, 1080-1088 (2008).
- ⁷ P. Achatz, J. A. Garrido, M. Stutzmann, O. A. Williams, D. M. Gruen, A. Kromka, and D. Steinmuller, *Appl. Phys. Lett.* **88**, 101908 (2006).
- ⁸ W. Gajewski, P. Achatz, O. A. Williams, K. Haenen, E. Bustarret, M. Stutzmann, and J. A. Garrido, *Phys. Rev. B* **79**, 045206 (2009).
- ⁹ M. Nesladek, K. Meykens, L. M. Stals, M. Vanecek, and J. Rosa, *Phys. Rev. B* **54**, 5552-5561 (1996).
- ¹⁰ Z. Remes, A. Kromka, J. Potmesil, and M. Vanecek, *Diamond Relat. Mater.* **17**, 1311-1315 (2008).
- ¹¹ C. E. Nebel, A. Waltenspiel, M. Stutzmann, M. Paul, and L. Schafer, *Diamond Relat. Mater.* **9**, 404-407 (2000).
- ¹² J. Alvarez, J. P. Kleider, P. Bergonzo, D. Tromson, E. Snidero, and C. Mer, *Diamond Relat. Mater.* **12**, 546-549 (2003).
- ¹³ R. Kravets, V. Ogorodniks, A. Poruba, P. Moravec, M. Nesladek, J. Rosa, and M. Vanecek, *Phys. Status Solidi A* **193**, 502-507 (2002).
- ¹⁴ P. Nemeč, J. Preclikova, A. Kromka, B. Rezek, F. Trojanek, and P. Maly, *Appl. Phys. Lett.* **93**, 083102 (2008).
- ¹⁵ J. Preclikova, F. Trojanek, A. Kromka, B. Rezek, B. Dzurnak, and P. Maly, *Phys. Status Solidi A* **205**, 2154-2157 (2008).

- ¹⁶ B. Dzurnak, F. Trojanek, J. Preclikova, A. Kromka, B. Rezek, and P. Maly, *Diamond Relat. Mater.* **18**, 776-778 (2009).
- ¹⁷ B. Dzurnak, F. Trojanek, J. Preclikova, A. Kromka, B. Rezek, and P. Maly, *Diamond Relat. Mater.* **20**, 1155-1159 (2011).
- ¹⁸ H. Kawarada and A. R. Ruslinda, *Phys. Status Solidi A-Apl. Mat.* **208**, 2005-2016 (2011).
- ¹⁹ S. D. Janssens, S. Drijkoningen, M. Saitner, H. G. Boyen, P. Wagner, K. Larsson, and K. Haenen, *J. Chem. Phys.* **137**, 044702 (2012).
- ²⁰ O. A. Williams, O. Douheret, M. Daenen, K. Haenen, E. Osawa, and M. Takahashi, *Chem. Phys. Lett.* **445**, 255-258 (2007).
- ²¹ S. D. Janssens, P. Pobedinskas, J. Vacik, V. Petrakova, B. Ruttens, J. D'Haen, M. Nesladek, K. Haenen, and P. Wagner, *New J. Phys.* **13**, 083008 (2011).
- ²² V. Seshan, D. Ullien, A. Castellanos-Gomez, S. Sachdeva, D. H. K. Murthy, T. J. Savenije, H. A. Ahmad, T. S. Nunney, S. D. Janssens, K. Haenen, M. Nesladek, H. S. J. van der Zant, E. J. R. Sudhölter, and L. C. P. M. de Smet, *J. Chem. Phys.* **138**, 234707 (2013).
- ²³ D. H. K. Murthy, T. Xu, W. H. Chen, A. J. Houtepen, T. J. Savenije, L. D. A. Siebbeles, J. P. Nys, C. Krzeminski, B. Grandidier, D. Stievenard, P. Pareige, F. Jomard, G. Patriarche, and O. I. Lebedev, *Nanotechnology* **22**, 315710 (2011).
- ²⁴ T. J. Savenije, P. van Veenendaal, M. P. de Haas, J. M. Warman, and R. E. I. Schropp, *J. Appl. Phys.* **91**, 5671-5676 (2002).
- ²⁵ T. J. Savenije, A. J. Ferguson, N. Kopidakis, and G. Rumbles, *J. Phys. Chem. C* **117**, 24085-24103 (2013).
- ²⁶ M. Geisler and T. Hugel, *Adv. Mater.* **22**, 398-402 (2010).
- ²⁷ Z. Sun, J. R. Shi, B. K. Tay, and S. P. Lau, *Diamond Relat. Mater.* **9**, 1979-1983 (2000).
- ²⁸ S. Michaelson, O. Ternyak, A. Hoffman, and Y. Lifshitz, *Appl. Phys. Lett.* **89**, 131918 (2006).

- ²⁹ A. C. Ferrari and J. Robertson, *Phys. Rev. B.* **61**, 14095-14107 (2000).
- ³⁰ F. B. Liu, J. D. Wang, B. Liu, X. M. Li, and D. R. Chen, *Diamond Relat. Mater.* **16**, 454-460 (2007).
- ³¹ S. M. Baker, G. R. Rossman, and J. D. Baldeschwieler, *J. Appl. Phys.* **74**, 4015-4019 (1993).
- ³² P. Hubik, J. J. Mares, H. Kozak, A. Kromka, B. Rezek, J. Kristofik, and D. Kindl, *Diamond Relat. Mater.* **24**, 63-68 (2012).
- ³³ M. C. Rossi, F. Spaziani, S. Salvatori, and G. Conte, *Phys. Status Solidi A-Appl. Mat.* **199**, 71-76 (2003).
- ³⁴ F. Maier, M. Riedel, B. Mantel, J. Ristein, and L. Ley, *Phys. Rev. Lett.* **85**, 3472-3475 (2000).
- ³⁵ C. E. Nebel, F. Ertl, C. Sauerer, M. Stutzmann, C. F. O. Graeff, R. Bergonzo, O. A. Williams, and R. B. Jackman, *Diamond Relat. Mater.* **11**, 351-354 (2002).
- ³⁶ V. Petrakova, A. Taylor, I. Kratochvilova, F. Fendrych, J. Vacik, J. Kucka, J. Stursa, P. Cigler, M. Ledvina, A. Fiserova, P. Kneppo, and M. Nesladek, *Adv. Funct. Mater.* **22**, 812-819 (2012).
- ³⁷ G. Speranza, S. Torrenzo, M. Filippi, L. Minati, E. Vittone, A. Pasquarelli, M. Dipalo, and E. Kohn, *Surf. Sci.* **604**, 753-761 (2010).
- ³⁸ L. Diederich, O. Kuttel, P. Aebi, and L. Schlapbach, *Surf. Sci.* **418**, 219-239 (1998).
- ³⁹ Z. Remes, R. Kalish, C. Uzan-Saguy, E. Baskin, M. Nesladek, and S. Koizumi, *Phys. Status Solidi A-Appl. Mat.* **199**, 82-86 (2003).
- ⁴⁰ W. Janssen, S. Turner, G. Sakr, F. Jomard, J. Barjon, G. Degutis, B. Ruttens, A. Hardy, M. van Bael, J. Verbeeck, G. van Tendeloo, and K. Haenen, submitted to *Applied Physics Letters* (2014).
- ⁴¹ B. Rezek, J. Cermak, A. Kromka, M. Ledinsky, and J. Kocka, *Diamond Relat. Mater.* **18**, 249-252 (2009).

Chapter 4

Electrical Characterization of Diamond Structures

Work in this chapter has been performed in collaboration with:

- C. R. Arroyo, S. Etaki, F. Prins, M. L. Perrin, M. Nesládek, E. J. R. Sudhölter, L. C. P. M. de Smet, H. S. J. van der Zant, and D. Dulić.

This chapter deals with the fabrication and electrical transport measurements of Hall bar structures manufactured from boron-doped nanocrystalline diamond thin films. The Hall bar structures are fabricated using standard lithography techniques. The electrical transport properties such as the magneto-resistance are measured in the temperature range of 20 mK to 5 K under perpendicular magnetic fields of up to ± 2.5 T. It is observed that the Hall bar devices made from the boron-doped diamond films show a critical field in the range of 1.5 T to 2.0 T and a critical current density in the range of 1.6×10^6 A/m² to 1.9×10^6 A/m² depending on the device geometry. The critical temperature of our devices is found to be between 1 and 2 K. Furthermore, the nanostructured devices

show a residual resistance below the critical temperature, which could be due to the presence of non-superconducting areas caused by a non-homogenous distribution of boron dopants. From the Hall measurements, the charge carrier density in these films is estimated to be $1.6 \times 10^{21} \text{ cm}^{-3}$.

4.1 Introduction

Carbon-based materials such as graphene, carbon nanotubes and diamond have been extensively studied in recent years due to their fascinating properties and potential applications.¹⁻⁵ Among them, diamond is a unique material due to its superior properties such as broadband optical transparency, chemical stability in aqueous environment, high thermal conductivity and bio-compatibility.⁵⁻⁷ As a result, diamond has been successfully utilized in making field-effect transistors, single-photon sources, (bio)sensors and nanoelectromechanical switches.⁸⁻¹¹ With the advancement in the chemical vapour deposition (CVD) technique, synthetic diamond thin films and especially, the nanocrystalline types can be produced with properties closely related to natural diamond.¹² Furthermore, the nanocrystalline diamond (NCD) thin films can be grown on different substrates such as silicon, glass, quartz, etc at a low-cost, which makes them attractive.^{13,14}

Intrinsic diamond is an electrical insulator. However, it can be doped with impurities such as boron atoms to tune its electronic properties from being insulating to semiconducting and (super)-conducting.^{15,16} At relatively low concentrations ($n_B \approx 10^{17} \text{ cm}^{-3}$) of boron, the diamond behaves as a p-type semiconductor whereas on increasing the boron concentration above a critical value of $n_c \approx 5 \times 10^{20} \text{ cm}^{-3}$, it undergoes a doping-induced metal-to-insulator transition.¹⁷ Depending on the boron concentration and crystal orientation of the diamond material, superconductivity at temperatures of up to 11 K has been observed.¹⁸ The granular nature of the NCD films together with the control over its dimensions and doping concentration make these films an appropriate platform to study superconducting mechanisms in disordered materials.^{15,19,20} As a first step towards a detailed investigation of superconductivity in disordered materials, it is important to develop a fabrication method to manufacture Hall bar structures/devices based on NCD films and characterize their electronics properties. The design and

fabrication of the Hall bar structures have several advantages. For instance, the Hall bar design allows electrical transport measurements in a four-terminal configuration eliminating contribution to the conductance of the contact resistance present in a two-terminal configuration. At low temperatures, the longitudinal voltage measurement can be used to study the superconducting behavior of the structures and their related parameters such as the critical temperature, the critical field and the critical current. In the normal state, the same Hall structures can be used to measure the transverse (Hall) voltage to estimate the charge carrier density in the films.

In this work, we present a fabrication method based on standard electron-beam (e-beam) lithography to fabricate Hall bar structures from boron-doped NCD thin films. The electrical transport properties of the Hall bar structures are measured in the temperature range of 20 mK to 5 K in the presence of perpendicular magnetic fields of up to ± 2.5 T. The Hall bar structures show critical fields and critical current densities in the range of 1.5 T to 2.0 T and 1.6×10^6 A/m² to 1.9×10^6 A/m², respectively. The critical temperature at which superconductivity starts to appear lies between 1 K and 2 K. In addition, these structures show a residual resistance below the critical temperature, which may be attributed to non-superconducting regions present in the Hall bar structures. The Hall measurements indicate a charge carrier density of 1.6×10^{21} cm⁻³.

4.2 Experimental

Boron-doped NCD films were grown on a silicon substrate with an oxide on top, using the microwave plasma-enhanced CVD technique.²¹ Before the start of the CVD growth process, the oxidized silicon substrate was cleaned and sonicated for 2 - 3 min in nitric acid; subsequently, the substrate was rinsed with deionized water. The substrate was then dip coated in a solution containing dia-

mond nanoparticles with sizes of 6 to 10 nm.²² The diamond nanoparticles deposited on the substrate act as nucleation centers for the formation of the diamond film. The thin films were grown inside the CVD reactor using a H₂/CH₄ plasma with a methane concentration around 3 %. In addition to H₂/CH₄ gases, trimethyl-boron gas (boron to carbon concentration ratio of ~3000 ppm) was introduced during the CVD growth process for boron doping in the film. The substrate temperature was maintained at 700 °C and the pressure was around 40 mbar.

Hall bar structures with different widths and lengths were fabricated from boron-doped NCD films using standard e-beam lithography. In Fig. 4.1, the schematic of the fabrication process is shown. To make Hall bar structures boron-doped NCD films were first spin-coated to form a double-layer resist, i.e., 330 nm of methyl-methacrylate (MMA, 17.5 %) and methacrylic acid (MAA, 8 %) copolymer followed by 250 nm of poly-MMA with a molecular weight of 950 kD. The sample was then prebaked at 175 °C for 12 min. The lower layer in the resist stack is more sensitive to the e-beam than the upper layer resist, which leads to an undercut on development of the pattern, thereby facilitating the lift-off process. The resists were exposed to an e-beam with a dose of 100 $\mu\text{C}/\text{cm}^2$ and an acceleration voltage of 100 kV. After e-beam lithography, development of the exposed areas was done by dipping the sample in a 1:3 mixture of methyl isobutyl ketone (MIBK) and isopropyl alcohol (IPA) for 2 min, followed by dipping the sample in IPA for 1 min. A thin layer of aluminum (~60 nm thick) was deposited using a standard e-beam evaporator, which served as a mask protecting the diamond film underneath it. The lift-off of the remaining resist was done in hot acetone. The etching of the diamond thin film was carried out using oxygen reactive ion etching (RIE) with a dc bias voltage of -413 V, a power of 30 W, an O₂ gas flow of 30 ml/min and a pressure of 20.7 μbar for 22 min. The protective aluminum layer was finally removed by wet chemical etching using a 0.8 wt% potassium hydroxide solution. In the

second step, the contact pads were fabricated by evaporation of titanium (20 nm) followed by 200 nm of gold.

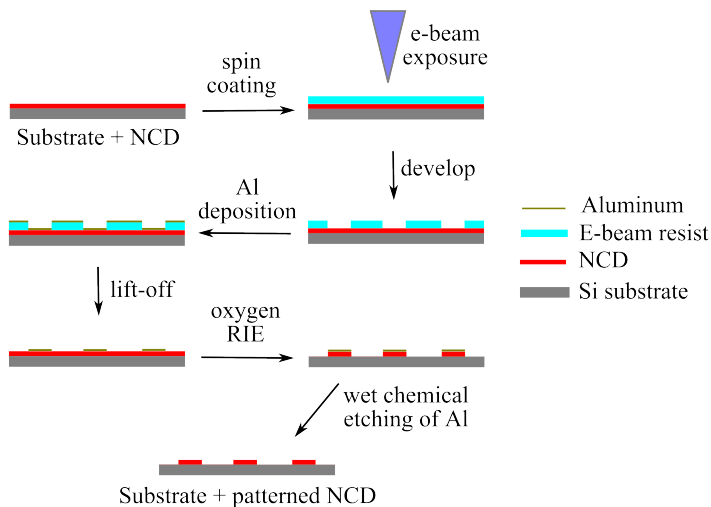


Figure 4.1: Schematics of the Hall bar fabrication process showing the steps in which the Hall bar geometry is transferred in the diamond films. The subsequent fabrication process of metal contacts/electrodes is not shown here.

4.3 Results and Discussion

We fabricated two Hall bar devices: one device with a 100 nm width and a 1.2 μm length and the other device with a 1000 nm width and a 2.9 μm length. Hereafter, these devices will be referred to as device A and device B, respectively. Figure 4.2(a) shows a scanning electron microscope (SEM) image of device B. The inset shows a higher magnification image of the film in which the nanocrystalline nature of the film can be easily observed. The thickness/height of the film was measured using an atomic force microscope and was found to be 180 nm (Fig. 4.2(b)). The electrical characterization of the devices was done by injecting a dc current along the longest dimension of the Hall bar while mea-

asuring the voltage across sets of voltage probes (Fig. 4.2(c)). The longitudinal voltage (V_{xx}) is measured by using the two voltage probes on the same side whereas the transverse (Hall) voltage (V_{xy}) is obtained by using the two voltage probes opposite from each other. Both voltages can be measured in the presence of magnetic field applied perpendicular to the sample. Two types of measurements were performed. For the first type of measurements, the superconducting behavior of the Hall structures was recorded by measuring the longitudinal voltage vs. current ($V_{xx}-I$) and the differential resistance ($dV_{xx}/dI-I$) simultaneously using a lock-in technique with an ac modulation current of 20 nA and a frequency of 73.68 Hz. These results were used to study the superconducting properties such as the critical temperature, the critical field and the critical current. For the second type of measurements, V_{xy} and V_{xx} of the same structures were measured simultaneously using standard $V-I$ characterization without lock-in technique to estimate the charge carrier density and magneto-resistance, respectively.

The four-terminal longitudinal resistances of the Hall bar devices measured at room temperature were 4.60 k Ω for device A and 1.26 k Ω for device B corresponding to a resistivity of 6.9×10^{-5} $\Omega\cdot\text{m}$ and 7.8×10^{-5} $\Omega\cdot\text{m}$, respectively. For electrical characterization at low temperature, the devices were cooled using a dilution refrigerator with a base temperature of 20 mK. Figure 4.3 (left panels) shows the $V-I$ characteristics measured at 5.4 K (red curve) and 20 mK (blue curve) for device A and device B. The devices behave as a normal conductor at 5.4 K while it shows signs of superconducting behavior at 20 mK. The right panels of Fig. 4.3 plot the corresponding $dV/dI-I$ characteristics measured at 20 mK (blue curve) for device A and device B. The $dV/dI-I$ characteristics show a suppressed resistance for low currents indicating the presence of superconducting correlations in the film. The position of the upward curvature to a higher resistance state can thus be identified as the critical current (I_c). For device A, I_c is ~ 19 nA

whereas for the device B, I_c is ~ 162 nA, corresponding to a critical current density of 1.9×10^6 A/m² and 1.6×10^6 A/m², respectively. We have also observed a hysteretic behavior between the forward and backward sweep (not shown in Fig. 4.3) due to most likely Joule heating, which has been previously reported in a similar type of structure.¹⁹ It is interesting to note that both devices show a residual resistance at zero current, whose value is smaller for device B as compared to device A. Finally, by measuring $V-I$ characteristics as a function of temperature, we found that the superconducting features disappear between 1 and 2 K. The critical temperature (T_c) thus lies in this range. A more accurate determination of T_c by systematically measuring $V-I$ characteristics in this range of temperatures has not been performed.

To study the influence of a magnetic field on the electronic properties of nanostructured boron-doped NCD films, the Hall bar devices were subjected to a perpendicular magnetic field ranging from -2.5 T to 2.5 T. Figure 4.4 shows $dV_{xx}/dI-I$ for device A (a) and device B (b) for five different values of the applied magnetic field. It is observed that the critical current decreases with an increase of the applied magnetic field. A rough estimate for the critical magnetic field (H_{c2}) at which superconductivity disappears and the material becomes a normal conductor can be obtained from these measurements; it is found to around 1.5 T for device A and around 2.0 T for device B. For negative magnetic fields in the range of 0 T to -2.5 T, the $dV_{xx}/dI-I$ characteristics (not shown) were found to be similar to the results presented here for the positive magnetic fields.

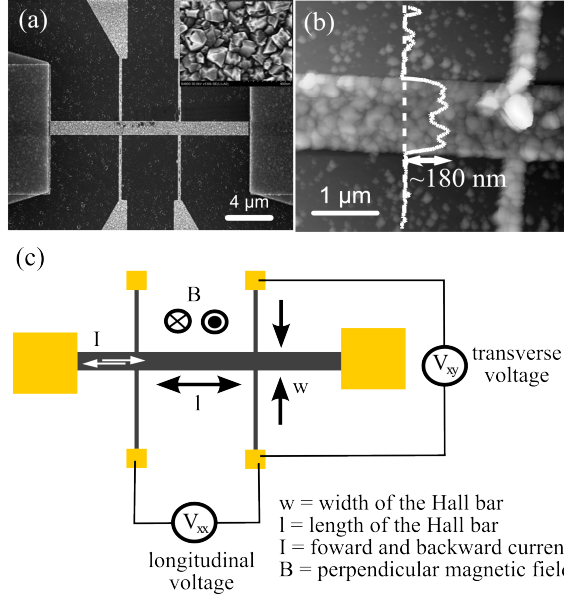


Figure 4.2: (a) Scanning-electron microscope (SEM) image of a Hall bar device with a 1000 nm width and a length of 2.9 μm (device B) fabricated from a boron-doped NCD film. The inset shows a higher magnification SEM image of a section of the film exhibiting the nanocrystalline nature of the film. (b) Atomic force microscope image of a section of device B showing the height/thickness profile (red line) measured along its 1000 nm width. (c) Scheme of the experimental setup used for the electrical transport measurements. A dc current is injected along the longest dimension of the Hall bar and the longitudinal (V_{xx}) and transverse (V_{xy}) voltages are measured in the presence of a perpendicular magnetic field. The yellow colored squares indicate the gold contact pads.

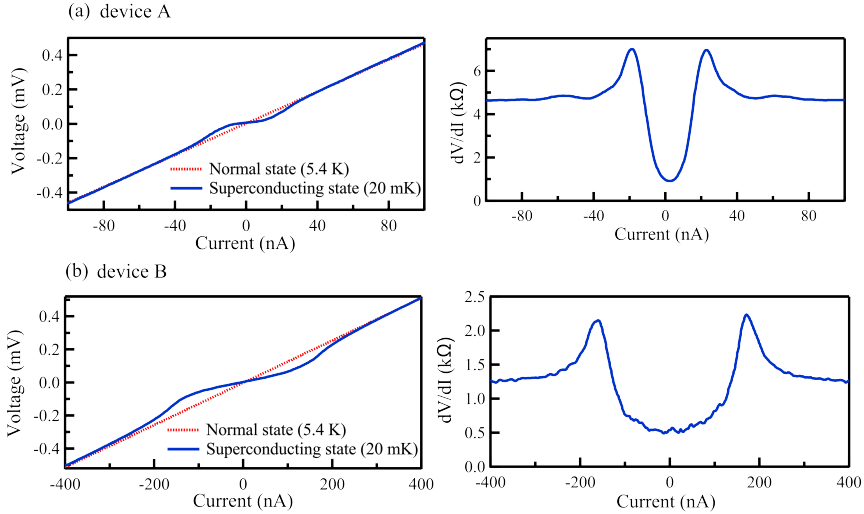


Figure 4.3: Longitudinal voltage (V_{xx}) vs. current of device A (a, top left panel) and device B (b, bottom left panel) measured at 5.4 K (red curves) and 20 mK (blue curves). The right panels show the corresponding differential resistance measured at 20 mK using a lock-in technique with an ac modulation current of 20 nA at 73.68 Hz.

In Fig. 4.5, we show the longitudinal resistance (V_{xx}/I) as a function of magnetic field (B) for device A (a) and device B (b). The longitudinal resistance was calculated from the longitudinal voltage that was measured using a standard V - I technique (without lock-in) at four different temperatures, i.e., 20 mK, 300 mK, 1 K and 5 K. The figures show that for high magnetic fields the curves saturate at the same value, which equals the normal-state resistance of the devices. Note, these values are close to the ones measured at room temperature indicating that the normal-state resistance is nearly temperature independent in the range between 20 mK $< T < 300$ K. Such a temperature dependence is generally attributed to conductors with a high degree of disorder. Figure 4.5 also shows that the resistance at $B = 0$ starts to decrease for temperatures below $T = 1$ K, in agreement with our

previous statement that T_c lies between 1 K and 2 K. The high degree of disorder may also explain why the resistance at low temperatures does not go to zero (residual resistance). The microscopic origin is not clear to us. It could be that the boron doping is inhomogeneous leaving parts of the film with a high resistance and /or that the granular structure of the films plays an important role.

Figure 4.6 shows the transverse (Hall) resistance (V_{xy}/I) as a function of magnetic field for device B. The transverse voltage was measured across the two voltage probes opposite to each other, in the presence of magnetic field applied perpendicular to the sample. From the Hall measurements in the normal state i.e., at 5 K, we can estimate the carrier density in the films. We first note that the Hall resistance is not zero at zero magnetic field; this can be explained by the granular nature of the films, which could lead to a situation in which the Hall voltage is not measured at positions that are exactly opposite to each other. As a result, a small contribution of the longitudinal resistance remains. Detailed inspection of Fig. 4.6 shows that the Hall resistance at 5 K increases linearly with increasing magnetic field; the value of R_{xy}/B is $0.021 \text{ } \Omega/\text{T}$. This is the expected Hall contribution and the charge carrier density (n) can be calculated as:

$$n = \frac{1}{et} \left[\frac{R_y}{B} \right]^{-1}, \quad (4.1)$$

where $e = 1.6 \times 10^{-19} \text{ C}$ and t is the thickness of the film (180 nm). With the experimental value of $0.021 \text{ } \Omega/\text{T}$, the carrier density in this equation is estimated to be $1.6 \times 10^{21} \text{ cm}^{-3}$, which agrees well with the reported value of $1.3 \times 10^{21} \text{ cm}^{-3}$ for a similar type of boron-doped nanocrystalline diamond film.²³ For device A, similar measurements have been performed. However, the data obtained was noisy making an accurate estimation of the carrier density difficult.

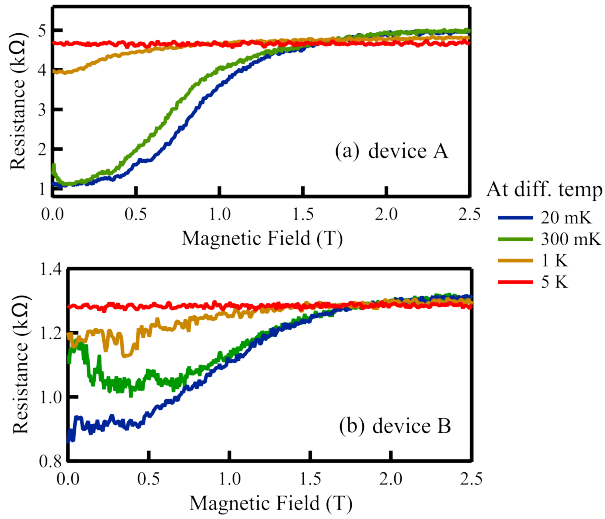


Figure 4.5: Four-terminal longitudinal resistance (V_{xx}/I) vs. magnetic field for device A (a) and device B (b) measured at four different temperatures, i.e., 20 mK, 300 mK, 1 K and 5 K. A positive magnetic field was applied perpendicular to the device. The current through the sample for these measurements was 100 nA for device A and 1 μ A for device B.

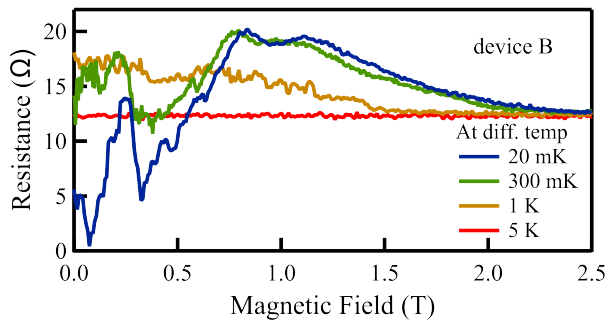


Figure 4.6: Transverse (Hall) resistance (V_{xy}/I) vs. magnetic field for device B measured at four different temperatures, i.e., 20 mK, 300 mK, 1 K and 5 K. The applied positive magnetic field was perpendicular to the device. The Hall resistance of the device tends to show fluctuations at 20 mK, 300 mK and 1 K up to 1.5 T. The current through the device B for this measurement was 1 μ A.

We also observe that for lower temperatures, the Hall resistance shows fluctuations up to 1.5 T beyond which the resistance saturates to normal state. Similar fluctuations were also observed for device A (data not shown). The origin of this anomalous behaviour is not understood and the analysis of the data is complicated given the granular nature of the films and the fact that the Hall resistance contains a substantial longitudinal component. More systematic studies would be needed to shed more light on this behavior.

4.4 Conclusion

To summarize, we have fabricated Hall bar devices of different dimensions from boron-doped nanocrystalline diamond thin films. These devices show a superconducting transition between 1 K - 2 K although at low temperatures a residual resistance remains. The critical current densities were measured to be of the order of 10^6 A/m² while the critical magnetic fields were found to be in range of 1.5 T - 2.0 T. These results provide important information on the electrical transport properties of nanostructured boron-doped diamond films and a starting point for more detailed studies of the superconducting properties of these films.

References

- ¹ A. K. Geim and K. S. Novoselov, *Nature Materials* **6**, 183-191 (2007).
- ² A. H. Castro Neto, F. Guinea, N. M. R. Peres, K. S. Novoselov, and A. K. Geim, *Rev. Mod. Phys.* **81**, 109-162 (2009).
- ³ R. H. Baughman, A. A. Zakhidov, and W. A. de Heer, *Science* **297**, 787-792 (2002).
- ⁴ S. J. Tans, A. R. M. Verschueren, and C. Dekker, *Nature* **393**, 49-52 (1998).
- ⁵ R. S. Sussmann, *CVD Diamond for Electronic Devices and Sensors*. (Wiley Publications, West Sussex, UK, 2009).
- ⁶ C. E. Nebel, D. C. Shin, B. Rezek, N. Tokuda, H. Uetsuka, and H. Watanabe, *J. R. Soc. Interface* **4**, 439-461 (2007).
- ⁷ J. E. Graebner, S. Jin, G. W. Kammlott, J. A. Herb, and C. F. Gardinier, *Appl. Phys. Lett.* **60**, 1576-1578 (1992).
- ⁸ H. Kawarada, M. Aoki, and M. Ito, *Appl. Phys. Lett.* **65**, 1563-1565 (1994).
- ⁹ C. E. Nebel, B. Rezek, D. Shin, H. Uetsuka, and N. Yang, *J. Phys. D-Appl. Phys.* **40**, 6443-6466 (2007).
- ¹⁰ T. M. Babinec, B. J. M. Hausmann, M. Khan, Y. A. Zhang, J. R. Maze, P. R. Hemmer, and M. Loncar, *Nat. Nanotechnol.* **5**, 195-199 (2010).
- ¹¹ M. Y. Liao, S. Hishita, E. Watanabe, S. Koizumi, and Y. Koide, *Adv. Mater.* **22**, 5393-5397 (2010).
- ¹² R. S. Balmer, J. R. Brandon, S. L. Clewes, H. K. Dhillon, J. M. Dodson, I. Friel, P. N. Inglis, T. D. Madgwick, M. L. Markham, T. P. Mollart, N. Perkins, G. A. Scarsbrook, D. J. Twitchen, A. J. Whitehead, J. J. Wilman, and S. M. Woollard, *J. Phys.-Condes. Matter* **21**, 364221 (2009).
- ¹³ M. Daenen, O. A. Williams, J. D'Haen, K. Haenen, and M. Nesladek, *Phys. Status Solidi A* **203**, 3005-3010 (2006).
- ¹⁴ O. A. Williams, *Diamond Relat. Mater.* **20**, 621-640 (2011).

- ¹⁵ M. Nesladek, D. Tromson, C. Mer, P. Bergonzo, P. Hubik, and J. J. Mares, *Appl. Phys. Lett.* **88**, 232111 (2006).
- ¹⁶ W. Gajewski, P. Achatz, O. A. Williams, K. Haenen, E. Bustarret, M. Stutzmann, and J. A. Garrido, *Phys. Rev. B* **79**, 045206 (2009).
- ¹⁷ E. Bustarret, P. Achatz, B. Sacepe, C. Chapelier, C. Marcenat, L. Ortega, and T. Klein, *Philos. Trans. R. Soc. A-Math. Phys. Eng. Sci.* **366**, 267-279 (2008).
- ¹⁸ Y. Takano, T. Takenouchi, S. Ishii, S. Ueda, T. Okutsu, I. Sakaguchi, H. Umezawa, H. Kawarada, and M. Tachiki, *Diam. Relat. Mat.* **16**, 911-914 (2007).
- ¹⁹ S. Mandal, C. Naud, O. A. Williams, E. Bustarret, F. Omnes, P. Rodiere, T. Meunier, L. Saminadayar, and C. Bauerle, *Phys. Status Solidi A* **207**, 2017-2022 (2010).
- ²⁰ B. L. Willems, G. Zhang, J. Vanacken, V. V. Moshchalkov, S. D. Janssens, K. Haenen, and P. Wagner, *J. Phys. D-Appl. Phys.* **43**, 374019 (2010).
- ²¹ S. D. Janssens, P. Pobedinskas, J. Vacik, V. Petrakova, B. Ruttens, J. D'Haen, M. Nesladek, K. Haenen, and P. Wagner, *New J. Phys.* **13**, 083008 (2011).
- ²² O. A. Williams, O. Douheret, M. Daenen, K. Haenen, E. Osawa, and M. Takahashi, *Chem. Phys. Lett.* **445**, 255-258 (2007).
- ²³ W. Gajewski, P. Achatz, O. A. Williams, K. Haenen, E. Bustarret, M. Stutzmann, and J. A. Garrido, *Physical Review B* **79**, 045206 (2009).

Chapter 5

Nanogap Formation in Diamond Structures

This chapter is based on the following publication:

- **V. Seshan**, C. R. Arroyo, A. Castellanos-Gomez, F. Prins, M. L. Perrin, S. D. Janssens, K. Haenen, M. Nesládek, E. J. R. Sudhölter, L. C. P. M. de Smet, H. S. J. van der Zant, and D. Dulic “*Current-induced nanogap formation and graphitization in boron-doped diamond films*” Applied Physics Letters, 2012 101(19): 195106.

A high-current annealing technique is used to fabricate nanogaps and hybrid diamond/graphite structures in boron-doped nanocrystalline diamond films. Nanometer-sized gaps down to ~1 nm are produced using a feedback-controlled current annealing procedure. The nanogaps are characterized using scanning electron microscopy and electronic transport measurements. The structural changes produced by the elevated temperature, achieved by Joule heating during current annealing, are characterized using Raman spectroscopy. The formation of hybridized diamond/graphite structure occurs at the point of maximum heat accumulation.

5.1 Introduction

During the last decade, carbon-based materials like diamond,¹ graphene² and carbon nanotubes (CNTs)³ have been extensively studied due to their outstanding physical properties and potential applications. Consequently, hybrid structures combining the advantages of different allotropes of carbon into one structure have gained interest. For instance, hybrid diamond/graphite structures can be relevant in molecular electronic applications because they benefit from both the robustness of sp^3 bonds and the flexibility of sp^2 hybridization for functionalization with a large variety of molecules. Hybrid structures such as diamond/graphite nanowires,⁴ diamond/graphite nanoflakes⁵ and diamond/CNTs⁶ composites have been reported in recent years.

So far these hybrid structures have been synthesized using the conventional plasma-based chemical vapor deposition (CVD) technique. This technique, however, does not allow in-situ fabrication of hybrid structures in specific domains. The current annealing technique,⁷ on the other hand, has proven to be effective to induce structural transformations and even to fabricate nanometer-sized gaps. For example, the transformation of amorphous carbon layers into graphene⁸ and restructuring of CNTs⁹ have been reported using this technique. Furthermore, high-current annealing has also been used to fabricate nanogaps in few-layer graphene¹⁰ and CNTs.¹¹ High-current annealing can therefore also be a promising technique to fabricate nanogaps and hybrid structures in diamond-based devices; this has not been explored yet.

Nanocrystalline diamond¹² films are unique due to their close resemblance to single-crystal diamond for many properties, the flexibility to grow on different substrates and the control over their electrical properties *via* boron doping (ranging from a wide band-gap insulator to semiconductor and superconductor). Boron-doped nanocrystalline diamond (B:NCD) films have been successfully implemented as an electrochemical electrode,¹³ sensor¹⁴ and even

superconducting quantum interference device (SQUID).¹⁵ However, engineering B:NCD for using it as a novel electrode material for molecular electronics applications has been a big challenge because the strong covalent carbon network of diamond requires an unconventional approach to structure it.

In this letter, we introduce a technique involving current-induced annealing to create nanogaps as well as hybrid B:NCD/graphite structures. Using a feedback control loop, current annealing can be used to create gaps down to ~ 1 nm. The structural change from diamond to a graphitic phase in B:NCD produced by the Joule heating during the current annealing is characterized by Raman spectroscopy. The results presented here offer a method to engineer diamond devices to incorporate hybrid diamond/graphitic structures and nanogaps which cannot be performed using alternative techniques.^{4,6}

5.2 Experimental

B:NCD films were grown on a silicon oxide substrate in an ASTeX 6500 series using microwave plasma-enhanced CVD technique. Prior to the CVD, a silicon substrate was cleaned with nitric acid in an ultrasonic bath for 2 - 3 min and then rinsed with deionized water. The substrate was then subsequently dip-coated in a colloidal solution containing detonation diamond with a particle size of 5 - 10 nm.¹⁶ The resulting layer of diamond particles on the substrate acts as a nucleation center. A thin film was grown from the seeded substrate inside a CVD reactor using an H_2/CH_4 plasma with a methane concentration around 3 vol%. The substrate temperature was maintained at 700 °C with process pressure of ~ 40 mbar and microwave power of 3500 W. Boron doping in the film was achieved by introducing trimethylboron (concentration ~ 3000 ppm) gas during the CVD process.¹⁷

B:NCD-based devices were fabricated from the film by using standard electron-beam lithography. First, the B:NCD film was

spin-coated with a double layer of resist, i.e., 330 nm of methylmethacrylate (MMA, 17.5 %) and methacrylic acid (MAA, 8 %) copolymer followed by 250 nm of poly-MMA with a molecular weight of 950 kD and then prebaked at 175 °C for ~12 min. The resists were exposed to the electron beam with a dose of 900 $\mu\text{C}/\text{cm}^2$ and an acceleration voltage of 100 kV. The development of the exposed areas was done by dipping the substrate in a 1:3 volume of methyl isobutyl ketone (MIBK) and isopropyl alcohol (IPA) for 2 min followed by IPA for 1 min. A thin layer of aluminium (60 nm thick) was deposited on the developed part of the resist by electron-beam evaporation followed by lift-off in hot acetone. The thin film was then etched using oxygen (O_2) reactive ion etching (RIE) with a DC bias voltage of -413 V, O_2 gas flow of 30 ml/min, pressure of 20.7 μbar and power of 30 W for ~22 min. The aluminium film acts as a mask during the etching process thereby protecting the diamond film/structures underneath. After the RIE process, the protective aluminium layer was removed using 0.8 wt% KOH solution. In a second lithographic step, contact pads of 20 nm titanium/200 nm gold were fabricated. In order to characterize the electron transport properties and nanogaps in B:NCD film, two batches of devices were fabricated. One batch consisted of a Hall bar geometry while the second batch consisted of 2-terminal geometry. After fabrication, the devices were characterized employing optical microscopy, atomic force microscopy (AFM), electrical transport measurements at low temperature, scanning electron microscopy (SEM) and Raman spectroscopy.

5.3 Results and Discussion

Figure 5.1(a) shows an optical micrograph using a 100 \times magnifying objective and (b) shows the corresponding SEM image of a device fabricated following the steps described above. The thickness of this B:NCD film/device has been measured by means of AFM (scanned area marked with the dashed square in Fig. 5.1(a))

and was found to be ~ 180 nm (Fig. 5.1(c)). The Hall bar devices were electrically characterized using a 4-terminal geometry in a $^3\text{He}/^4\text{He}$ dilution refrigerator with a base temperature of 20 mK by injecting a DC current and measuring the voltage drop across two electrodes. Figure 5.1(d) presents the current vs. voltage characteristics for a device at 5.4 K (red curve) and 54 mK (blue curve). While at 5.4 K the device behaves as an ohmic conductor, at 54 mK the transport characteristics show signs of superconducting behavior.¹⁸ For this device, the critical current was found to be ~ 100 nA. The onset of superconductivity for our B:NCD devices was found to be between 1 and 2 K (see also Chapter 4).

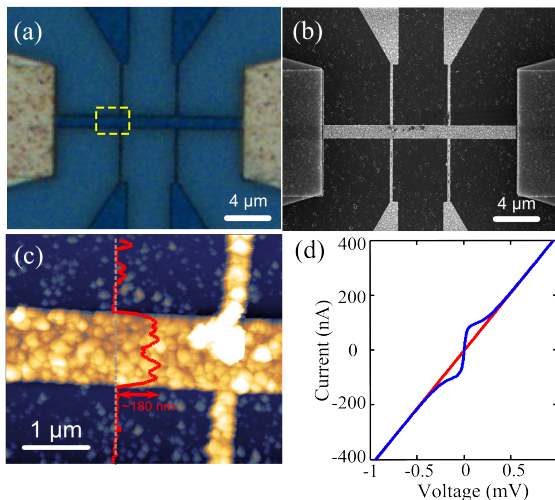


Figure 5.1: (a) Optical image using a $100\times$ magnifying objective marked with AFM scan area (dashed square) and (b) corresponding SEM image of the device fabricated on the B:NCD film. (c) Topography AFM image of the device with height profile (red curve). (d) Current vs. voltage characteristics of the device measured at 5.4 K (red curve) and 54 mK (blue curve).

B:NCD devices were then subjected to high-current annealing in air at room temperature using a feedback-controlled scheme, as

shown in Fig. 5.2(a). Although the devices were fabricated in a Hall bar geometry, for current annealing they were used in 2-terminal geometry. A voltage (V) ramp with a rate of 1 V/s was applied to the device while the current (I) was measured every 100 μ s. The high currents are used to create voids in the diamond wires and to eventually break them. If the conductance (I/V) dropped more than 10 % within a 200 mV range, the voltage was swept back to zero after which a new ramp was started. This process was repeated until a gap was formed (Fig. 5.2(b)). Figure 5.2(c) shows a typical I - V graph of the feedback-controlled high-current annealing process. The current increases with the voltage until a critical point where the conductance starts to decrease (indicated by the red circles in Fig. 5.2(c)). The arrow in Fig. 5.2(c) indicates the evolution of the I - V traces after sequential high-current annealing steps, eventually leading to the formation of a nanogap. The nanogaps in the first batch of B:NCD devices were found to be separated by \sim 100 nm; gap formation occurred approximately in the middle of the diamond wire.

During the high-current annealing, the film heats up which may lead to structural changes. In order to gain a deeper insight into the structural changes induced by the high-current annealing, Raman spectroscopy has been employed. This technique has been extensively used to study different allotropic forms of carbon-based materials.^{19,20} A micro-Raman spectrometer (Renishaw in via RM 2000) was used in a backscattering configuration excited with visible laser light ($\lambda = 514$ nm). The spectra were collected through a $100\times$ magnifying objective and recorded with 1800 lines/mm grating providing a spectral resolution of \sim 1 cm^{-1} . Before the high-current annealing, the B:NCD devices show all the typical features of boron-doped nanocrystalline diamond, i.e., peaks around 1300 and 1590 cm^{-1} , ascribed to the diamond and G band, in addition to another peak around 1210 cm^{-1} attributed to boron doping in diamond (Fig. 5.3(a)).^{21,22} The presence of a marginal G peak in the Raman spectrum is due to the presence of graphitic phases at the

grain boundaries. The peak below 1000 cm^{-1} corresponds to the excitation of a second order phonon in the silicon which was used as the substrate to grow B:NCD film.²¹

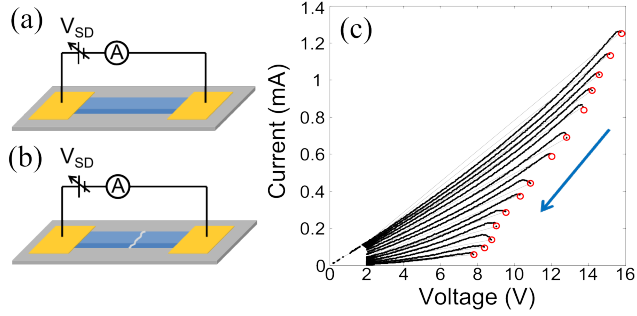


Figure 5.2: Schematic diagram of the feedback-controlled, high-current annealing process, before (a) and after (b) the formation of a nanometer-sized gap in the B:NCD device. (c) I - V graph of feedback-controlled, high-current annealing process. The red circles indicate a decrease in conductance while the arrow indicates the evolution of the I - V traces after sequential high-current annealing steps leading to a nanogap eventually.

After the high-current annealing, on the other hand, the Raman spectrum measured close to the nanogap changes drastically (Fig. 5.3(a)). The peak at 1590 cm^{-1} is more pronounced after current annealing and a new peak at 1347 cm^{-1} (D peak) is present, typically associated with the presence of sp^2 hybridized carbon.¹⁹ Therefore, the Raman spectra after the current annealing and near the nanogap resemble that of a graphitic phase, dominated by sp^2 instead of sp^3 hybridization. Such features have previously been observed for graphitized amorphous carbon samples subjected to high-temperature annealing, where the appearance of these features was attributed to a conversion from sp^3 to sp^2 hybridization.¹⁹ In the case of current-induced annealing, the B:NCD samples experience Joule heating due to the large current flow through the device ($\sim 1.2 \times 10^7\text{ A/cm}^2$). The highest temperature is reached in

the central part between the drain and source leads since the (gold) electrodes/contacts act as a heat-sink. Indeed, the graphitic-like Raman spectrum is not observed in the close vicinity of the electrodes where the increase of temperature is lower due to efficient heat dissipation to the electrodes.

The spatial distribution of the structural changes induced by high-current annealing has been studied by performing scanning Raman spectroscopy. The inset in Fig. 5.3(b) shows an optical image of a B:NCD device which has been subjected to the current annealing procedure resulting in a wide gap (~ 100 nm). Scanning Raman spectroscopy (laser spot size ~ 400 nm) has been carried out in the region highlighted with the dashed square. Figures 5.3(b)-(d) shows the intensity profile of the Raman peak at 1211 cm^{-1} (boron peak), 1347 cm^{-1} (D peak) and 1590 cm^{-1} (G peak) respectively. From these figures, one can conclude that the graphitic phases are located around the gap, indicating that the temperature at that spot reached an elevated temperature during the current annealing. Notice that similar graphitization processes have been achieved by annealing amorphous carbon¹⁹ and nanodiamonds^{23,24} around $1000\text{ }^\circ\text{C}$. This gives an estimation of the temperature reached in our device during our current annealing. The boron peak, on the other hand, shows a homogeneous intensity all along the device except for the gap region where the material has been removed by the current annealing process. However, due to the laser spot size (~ 400 nm) and the possible light scattering close to the gap edges, one cannot characterize structures below 200 nm and thus the gap cannot be successfully resolved by scanning Raman spectroscopy. Interestingly, we have observed graphitic-like Raman spectrum in some regions far from the gap (see the right side of the central bar in Figs. 5.3(c) and (d)), which suggests that these locations have experienced high temperature during the current annealing.

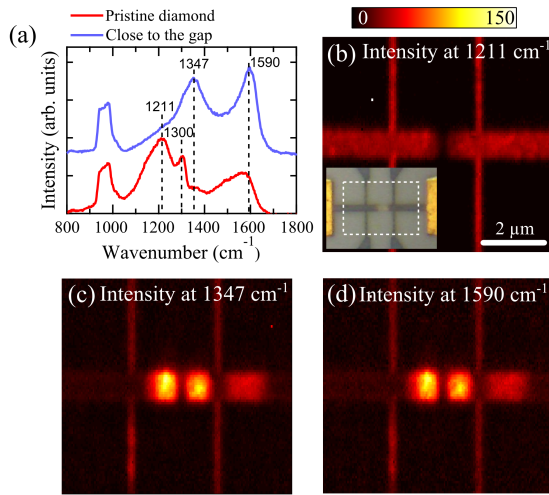


Figure 5.3: (a) Raman spectra of the pristine B:NCD film (red curve) and close to the gap (blue curve) after high-current annealing process. Spatial map of the intensity of the Raman peak at 1211 cm^{-1} (b) with inset showing the laser scanning area (white dashed square) on the device at 1347 cm^{-1} (c) and at 1590 cm^{-1} (d).

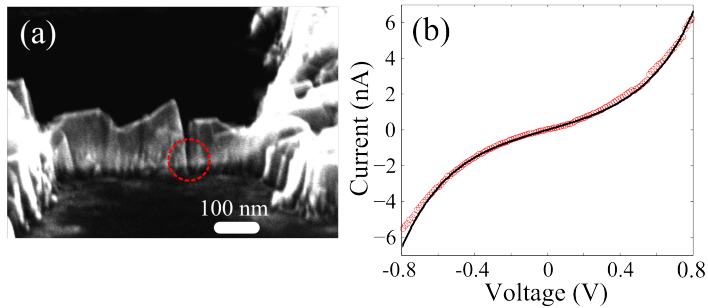


Figure 5.4: (a) Higher magnification SEM image (with false colored silicon oxide substrate) of one of the fabricated gaps in the B:NCD device. The red dotted circle indicates possible tunneling region. (b) I - V characteristics across the nanogap (red curve) and corresponding fit using the Simmons model for tunneling (black curve). Fit parameters used in Simmons model are area (A): 900 nm^2 , barrier height (ϕ): 1.15 eV and gap size (z): 1.42 nm.

While for the first batch of B:NCD devices the gap size was in the 100 nm range, a second batch of devices, with a 2-terminal geometry and smaller cross section area ($100 \times 100 \text{ nm}^2$), yielded a more controlled, high-current annealing process with smaller gaps in the 1 – 10 nm range. Overall, we have performed current annealing on 19 devices of which 15 devices showed a low-bias resistance in the range of $30 \text{ M}\Omega$ - $30 \text{ G}\Omega$ while the remaining four had an infinite resistance ($> 100 \text{ G}\Omega$). After current-induced annealing, the samples have been inspected using SEM (Hitachi high resolution FE-SEM (S-4800)). Figure 5.4(a) shows a close up SEM image of a nanogap. The SEM image illustrates how the nanogap is “wedge” shaped, being narrower at the bottom part where the electrodes are very close ($\sim \text{nm}$ range) and the tunneling process takes place. Quantitative analysis of top-view and high-angle SEM images gives an estimate of the tunneling area of $30 \times 30 \text{ nm}^2$. Figure 5.4(b) shows a typical tunneling I - V trace (red curve) measured at room temperature across one of the 15 devices annealed until opening a narrow nanogap/junction (see Appendix B). The tunneling phenomenon is an indication that the gap size is in the order of 1 - 2 nm as estimated using Simmons model²⁵ (fit shown as black curve in Fig. 5.4(b)). The parameters used in the fit are for the area (A): 900 nm^2 ($30 \times 30 \text{ nm}^2$), barrier height (ϕ): 1.15 eV and gap size (z): 1.42 nm. Although the barrier height is expected to be similar to the work function ($\sim 4 \text{ eV}$), for electron tunneling under ambient conditions, lower values (around 1 eV) have been observed for other carbon-based materials such as graphene nanogaps¹⁰ and carbon fiber-based scanning tunneling tips.²⁶ This procedure, therefore, can be used to fabricate nanometer-spaced electrodes and to engineer hybrid diamond/graphitic structures at specific places in the device.

5.4 Conclusion

We presented a study on the current-induced annealing in boron-doped nanocrystalline diamond devices. Using a feedback control loop, the current annealing technique can be used to create nano-sized gaps down to ~ 1 nm. The structural changes produced by the current-induced heating have been studied by Raman spectroscopy. We found that Joule heating increases the temperature enough to change the hybridization of diamond, dominated by sp^3 , to a graphitic sp^2 hybridized. The study reported here presents a novel way to engineer diamond-based devices into hybrid diamond/graphitic structures, with prospective use as nanoelectrodes, for instance in the field of molecular electronics.

References

- ¹ R. S. Balmer, J. R. Brandon, S. L. Clewes, H. K. Dhillon, J. M. Dodson, I. Friel, P. N. Inglis, T. D. Madgwick, M. L. Markham, T. P. Mollart, N. Perkins, G. A. Scarsbrook, D. J. Twitchen, A. J. Whitehead, J. J. Wilman, and S. M. Woollard, *J. Phys.-Condes. Matter* **21**, 364221 (2009).
- ² M. J. Allen, V. C. Tung, and R. B. Kaner, *Chem. Rev.* **110**, 132-145 (2010).
- ³ L. B. Hu, D. S. Hecht, and G. Gruner, *Chem. Rev.* **110**, 5790-5844 (2010).
- ⁴ I. L. Vlasov, O. I. Lebedev, V. G. Ralchenko, E. Goovaerts, G. Bertoni, G. Van Tendeloo, and V. I. Konov, *Adv. Mater.* **19**, 4058-4062 (2007).
- ⁵ J. K. Lee and P. John, *Thin Solid Films* **519**, 625-629 (2010).
- ⁶ X. C. Xiao, J. W. Elam, S. Trasobares, O. Auciello, and J. A. Carlisle, *Adv. Mater.* **17**, 1496-1500 (2005).
- ⁷ J. Moser, A. Barreiro, and A. Bachtold, *Appl. Phys. Lett.* **91**, 163513 (2007).
- ⁸ A. Barreiro, F. Borner, S. M. Avdoshenko, B. Rellinghaus, G. Cuniberti, M. H. Rummeli, and L. M. K. Vandersypen, *Scientific Reports* **3**, 1115 (2013).
- ⁹ O. Suekane, A. Nagataki, and Y. Nakayama, *Appl. Phys. Lett.* **89**, 183110 (2006).
- ¹⁰ F. Prins, A. Barreiro, J. W. Ruitenber, J. S. Seldenthuis, N. Aliaga-Alcalde, L. M. K. Vandersypen, and H. S. J. van der Zant, *Nano Lett.* **11**, 4607-4611 (2011).
- ¹¹ C. W. Marquardt, S. Grunder, A. Blaszczyk, S. Dehm, F. Henrich, H. von Lohneysen, M. Mayor, and R. Krupke, *Nat. Nanotechnol.* **5**, 863-867 (2010).
- ¹² O. A. Williams, *Diamond Relat. Mater.* **20**, 621-640 (2011).
- ¹³ Y. L. Zhou, J. F. Zhi, Y. S. Zou, W. J. Zhang, and S. T. Lee, *Anal. Chem.* **80**, 4141-4146 (2008).

- ¹⁴ J. W. Zhao, D. H. Wu, and J. F. Zhi, *J. Electroanal. Chem.* **626**, 98-102 (2009).
- ¹⁵ S. Mandal, T. Bautze, O. A. Williams, C. Naud, E. Bustarret, F. Omnes, P. Rodiere, T. Meunier, C. Bauerle, and L. Saminadayar, *ACS Nano* **5**, 7144-7148 (2011).
- ¹⁶ O. A. Williams, O. Douheret, M. Daenen, K. Haenen, E. Osawa, and M. Takahashi, *Chem. Phys. Lett.* **445**, 255-258 (2007).
- ¹⁷ S. D. Janssens, P. Pobedinskas, J. Vacik, V. Petrakova, B. Ruttens, J. D'Haen, M. Nesladek, K. Haenen, and P. Wagner, *New J. Phys.* **13**, 083008 (2011).
- ¹⁸ M. Nesladek, D. Tromson, C. Mer, P. Bergonzo, P. Hubik, and J. J. Mares, *Appl. Phys. Lett.* **88**, 232111 (2006).
- ¹⁹ A. C. Ferrari and J. Robertson, *Physical Review B* **64**, 075414 (2001).
- ²⁰ M. S. Dresselhaus, A. Jorio, M. Hofmann, G. Dresselhaus, and R. Saito, *Nano Lett.* **10**, 751-758 (2010).
- ²¹ P. Gonon, E. Gheeraert, A. Deneuve, F. Fontaine, L. Abello, and G. Lucazeau, *J. Appl. Phys.* **78**, 7059-7062 (1995).
- ²² S. Praver and R. J. Nemanich, *Philos. Trans. R. Soc. Lond. Ser. A-Math. Phys. Eng. Sci.* **362**, 2537-2565 (2004).
- ²³ S.P. Adiga, L.A. Curtiss, and D.M. Gruen, *Nanodiamonds* 35-54 (2010).
- ²⁴ J. Chen, S. Z. Deng, J. Chen, Z. X. Yu, and N. S. Xu, *Appl. Phys. Lett.* **74**, 3651-3653 (1999).
- ²⁵ J. G. Simmons, *J. Appl. Phys.* **34**, 1793-1803 (1963).
- ²⁶ A. Castellanos-Gomez, N. Agrait, and G. Rubio-Bollinger, *Nanotechnology* **21**, 145702 (2010).

III

Mechanics Section

Chapter 6

Fabrication and Characterization of Diamond Resonators

This chapter is based on the following work:

- **V. Seshan**, R. van Leeuwen, W. J. Venstra, B. Schneider, S. D. Janssens, M. Nesládek, K. Haenen, E. J. R. Sudhölter, L. C. P. M. de Smet, H. S. J. van der Zant, G. A. Steele, and A. Castellanos-Gomez “*Stamp-transfer fabrication of nanocrystalline diamond mechanical resonators*” In preparation.

An all-dry (no solvent), lithography-free stamp-transfer technique to fabricate diamond nanomechanical resonators is presented. Freely suspended nanocrystalline diamond drum structures ranging from 185 nm down to 55 nm thick are produced using this technique and their resonance characteristics are studied using an optical interferometer. These resonators reveal quality factors of 40 - 155 and resonance frequencies in the range 5 to 20 MHz

depending on their geometry. The stamp transfer technique is economical, quick and easy with 100 % yield.

6.1 Introduction

Nanoelectromechanical systems (NEMS) are enabling the next-generation sensors and actuators by coupling electrical and mechanical features at the nanometer scale.^{1,2} For further developments in NEMS applications, advanced materials with enhanced properties are being pursued. Diamond offers excellent mechanical, thermal and optical properties, such as a high Young's modulus, a high thermal conductivity and broadband transparency.³ Pristine or undoped diamond is electrically insulating. It can however be turned into a semiconductor or (super)conductor by adding dopants such as boron, rendering diamond-based structures to be incorporated as functional components in electronic circuits.^{4,5} In addition to being biologically compatible and inert to harsh environments, diamond can be functionalized chemically in an expansive manner.⁶ Moreover, diamond films such as nanocrystalline types can be grown over large areas on non-diamond substrates; this significantly reduces the production cost.⁷ These attractive properties and the fidelity of diamond open new avenues for NEMS applications, which include high-quality nanophotonic circuits, ultra-sensitive force and mass transducers operating under extreme conditions, and bio-nanomechanical devices.⁸⁻¹² For many of these applications, a diamond structure needs to be free-standing, and therefore it should be suspended from a substrate. To date, such suspended diamond structures, or resonators, have been fabricated using a top-down approach, which involves lithography, wet-chemical processing and critical-point drying.¹³⁻¹⁶

Here, we propose a lithography-free method to fabricate nanomechanical resonators, based on nanocrystalline diamond (NCD) films.⁷ The process is based on an all-dry (solvent-free) transfer technique, which allows the fabrication of ultra-thin devices and has the potential to be extended to an industrial scale. We demonstrate the fabrication of NCD nanomechanical drum resonators ranging in thickness from 185 nm down to 55 nm, with funda-

mental resonance frequencies in the range of 5-20 MHz and quality (Q) factors of 40 - 155, measured in vacuum at room temperature. The stamping technique presented here can be used to transfer conducting as well as non-conducting materials. Since there is no wet-chemical processing step involved, it can be efficiently used as a final fabrication step. This opens new perspectives, e.g. to couple high-Q, conducting nanomechanical resonators to pre-designed electronic circuits/devices in resonator-coupled qubit circuits.^{17,18} Furthermore, unlike most studies on NCD resonators that focus on cantilever geometries, we investigate the drum configuration, which has not been explored so far using NCD.^{14,19,20} Drum resonators are interesting as they can be mechanically stable at thicknesses down to a single atom due to their clamped geometry around the perimeter.^{21,22}

6.2 Experimental

Prior to the microwave plasma-enhanced CVD process, the quartz substrates were seeded with diamond nanoparticles (5 - 10 nm in diameter).²³ The deposition of the NCD films was carried out using a conventional H_2/CH_4 plasma with a methane concentration of $\sim 4\%$ (v/v). The microwave power was maintained at 3500 W, the substrate temperature at 510 - 560 °C and the process pressure at 33 - 40 mbar. The thickness of the NCD film was monitored in-situ using a laser interferometer. The CVD growth process was stopped when the thickness of the film reached a value of 180 nm. At this thickness, in combination with well-chosen conditions, the NCD films start to delaminate from the quartz substrate, forming numerous flakes. These flakes remain weakly adhered to the quartz surface.

To estimate the thickness of the NCD flakes, tapping-mode atomic force microscopy (AFM) was performed using a Digital Instruments D3100 AFM with a standard silicon cantilevers (spring constant of 40 N/m and tip curvature < 10 nm).

The thinning procedure was carried out on the NCD flakes that are weakly adhered to the quartz substrate prior to the stamping process. The NCD flakes were thinned down using an oxygen (O_2) reactive ion etching (RIE) in a Leybold Hereaus system with a DC bias voltage of -413 V, an O_2 gas flow of 30 ml/min and a pressure of ~ 20.7 μ bar for ~ 10 min. This results in an etching rate of 15 nm/min. The NCD flakes that were 185 nm thick initially were reduced to 55 nm. Note that during RIE, the top side of the flake undergoes thinning while the opposite side of the flake, which is in contact with the quartz substrate, remains mostly unaffected.

The mechanical motion of the NCD membrane was measured using an optical interferometer, as described in more detail previously.^{22,24} Briefly, the setup consists of a Helium-Neon probing laser ($\lambda = 632.8$ nm) focused on the suspended part of the membrane and a blue diode laser ($\lambda = 405$ nm) with an optical output below 1 mW for photothermal excitation of the resonators. While the pre-patterned silicon surface with a hole acts as the fixed mirror, the flake itself acts as the semi-transparent moving mirror, thus forming an interferometer. On photothermal excitation, the motion of the NCD membrane changes the distance between the mirrors and, via constructive or destructive interference, modulates the reflected optical power. The intensity of the reflected optical signal is detected using a photodiode. All the measurements were carried out in vacuum ($\sim 10^{-5}$ mbar) to reduce damping from ambient gas molecules.

6.3 Results and Discussion

Figure 6.1(a) shows an optical image of the quartz surface supporting the delaminated NCD flakes. In the first step, a transparent visco-elastic stamp (GelFilm® by GelPak), similar to those used in nano-imprinting, is brought into contact with the sample supporting the NCD flakes using a micromanipulator.²⁵ Once in contact, due to the visco-elasticity, the stamp material can follow

the topography of the NCD flakes that are weakly adhered to the substrate. When the stamp is peeled-off rapidly, NCD flakes are transferred from the (substrate) surface onto the stamp. Figure 6.1(b) shows the optical image of the same sample after peel-off, which displays loss of flakes from the sample surface. In order to fabricate the NCD mechanical resonators, the NCD flakes are transferred from the stamp to another surface pre-patterned with holes of different diameters. Figure 6.1(c) shows an example of a pre-patterned hole with a diameter of 15 μm , on a silicon substrate with an oxide on top (SiO_2). Note that one could use any commercially available pre-patterned substrate such as TEM grids or microfilters to fabricate these mechanical resonators.²⁶ The stamp was mounted in a 3-axis micromanipulator with the surface containing the NCD flakes facing the substrate, and aligned over the desired (hole) structure under a zoom lens (Fig. 6.1(d)). By lowering the manipulator, the stamp is first brought into contact with the substrate and then pressed slightly against the substrate. This step is followed by a slow peel-off process (approx. 5 - 10 min) using the micromanipulator, which transfers the NCD flake over the hole and results in a freely-suspended mechanical structure.²² Figure 6.1(e) - (h) shows the transfer process of the flake from the visco-elastic stamp to the SiO_2 substrate with the hole. Figure 6.1(h) shows one such freely suspended NCD flake/resonator. The whole manufacturing process of peeling off and transfer of flakes is accomplished in 10 - 15 min. The transparency of the visco-elastic stamp allows precise positioning of the flake over the holes by monitoring and adjusting their relative position using an optical microscope.

After the fabrication of the NCD mechanical resonators, the (resonator) devices are characterized using AFM. The thickness of the NCD resonator shown in Fig. 6.1(h) is found to be 185 nm (see Appendix C). By RIE in an O_2 plasma (details on thinning of NCD flakes are provided in the above experimental section), we found that the NCD flakes can be controllably thinned down by 130 nm

at a rate of 15 nm/min to a thickness of 55 nm. The RIE thinning procedure was performed prior to the stamping process, while the NCD flakes are adhered to the quartz substrate.

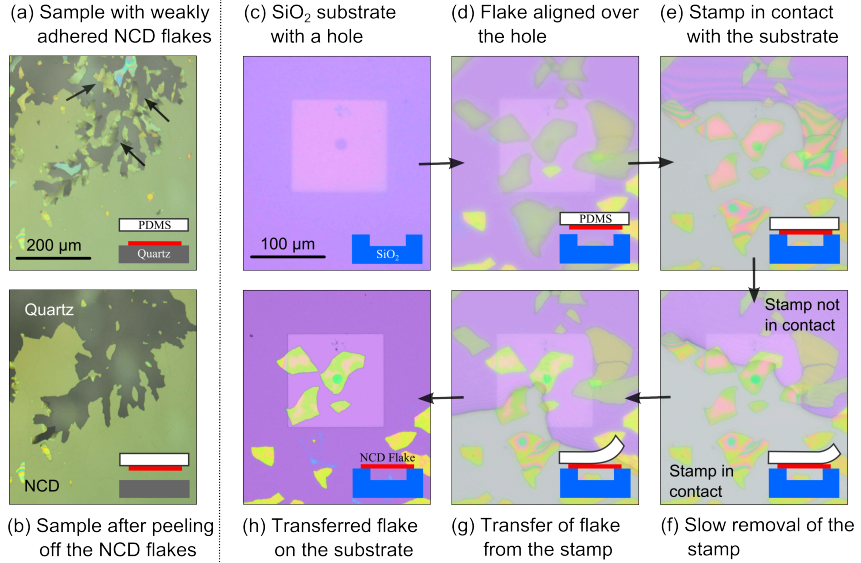


Figure 6.1: Optical microscopy images of the NCD flakes on the quartz substrate (a) before and (b) after stamping with a visco-elastic material. The arrows in panel (a) indicate the NCD flakes weakly adhered to the quartz substrate. (c) - (h) Series of optical microscopy images: (c) a pre-patterned SiO₂ substrate with a hole (diameter: 15 μm); (d) the selected NCD flake aligned over the hole on a SiO₂ substrate using the micromanipulator; (e) - (g) the stamp brought in contact with the substrate and peeled-off using the micromanipulator; (h) the NCD flake/-resonator suspended over the hole on a SiO₂ substrate. The inset shows a schematic of the stamping process.

Note that the transfer method including RIE is all-dry and no solvent is used throughout the manufacturing process. Thus, in contrast to typical wet-etching techniques for mechanical resonator fabrication, which require critical-point drying to avoid the collapse of the suspended structures by capillary forces, the present tech-

nique provides a practical and straightforward route towards suspended nanomechanical resonators.¹³ With our stamping technique, we achieve 100 % success rate for five manufactured devices with thicknesses of ~ 55 nm and ~ 185 nm and diameters from 6 μm to 15 μm .

The resonant motion of the NCD resonators was detected using an optical interferometer.^{22,24} Figure 6.2 shows the measured mechanical magnitude (circles) and phase (squares) spectra, with the corresponding optical microscopy image for the devices with a thickness of 55 nm and varying (hole) diameters of 15 μm , 10 μm , 8 μm and 6 μm . The resonance frequencies and Q-factors were extracted by fitting the data to a damped-harmonic oscillator model, indicated by solid lines in Fig. 6.2. The resonance frequency of the devices is found to be in the range of 5 to 20 MHz (depending on thickness and diameter), with Q-factors between 40 - 155. For devices with identical thickness measured under the same experimental conditions, we observe a significant increase of the Q-factor with the resonator diameter. This suggests that the Q-factor is limited by clamping losses. We note that similar resonance frequencies and Q-factors are observed for devices with identical geometries and dimensions, but made from different 2D materials, such as molybdenum disulfide (MoS_2).²⁷

To characterize our NCD resonators further, the resonance frequency (f_0) is measured as a function of the resonator thickness (t) and diameter (d). Figure 6.3(a) shows the measured resonance frequency versus the (resonator) thickness over the square of hole diameter for 55 nm and 185 nm thick NCD mechanical resonators. The uncertainty shown in the error bar in Fig. 6.3(a) is attributed to the roughness of the NCD flake, which is ± 15 nm (see Appendix C). For a plate-like circular resonator clamped around its perimeter, the frequency is given by:²⁸

$$f_0 = \frac{10.21}{\pi} \sqrt{\frac{E}{3\rho(1-\nu^2)}} \frac{t}{d^2}, \quad (6.1)$$

where E is the Young's modulus, ρ is the mass density and ν is the Poisson's ratio.

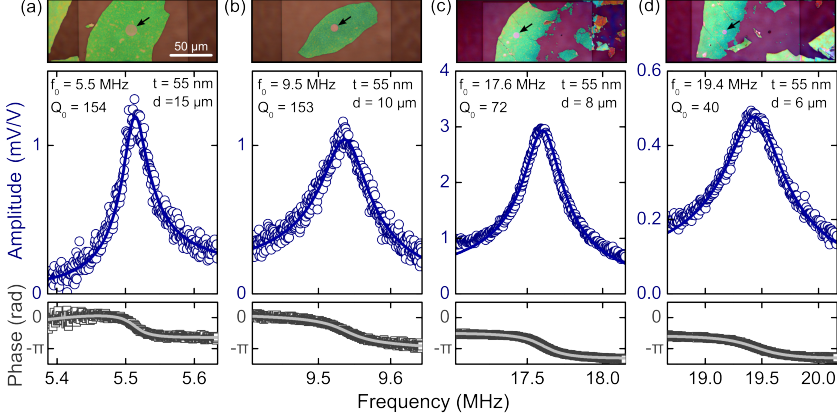


Figure 6.2: Measured normalized amplitude and phase response with corresponding optical image for the NCD mechanical resonators on a pre-patterned SiO_2 substrate with a (hole) diameter of (a) $15 \mu\text{m}$, (b) $10 \mu\text{m}$, (c) $8 \mu\text{m}$ and (d) $6 \mu\text{m}$. The arrow in the optical images indicates the location of the NCD mechanical resonators. The measured data (magnitude and phase) have been fitted to a damped-driven harmonic oscillator model (solid lines) to obtain their resonance frequency and quality factor.

For typical values for polycrystalline diamond of E ($\approx 304 \text{ GPa}$)²⁹, ρ ($3500 \text{ kg}\cdot\text{m}^{-3}$)²⁹ and ν (0.12)³⁰, the resonance frequencies calculated from Equation (6.1) are shown by the central solid line in Fig. 6.3(a). The good correspondence between the measured data and this solid line indicates that the resonators indeed behave as circular plates whose dynamics is thus dominated by the bending rigidity and not by their initial pre-tension. This is a desirable feature for nanomechanical resonators as the bending rigidity can be easily controlled by geometrical factors while the initial pre-tension typically varies from device to device. For a pre-tension dominated device, the second order eigenmode is expected to be at $1.59 f_0$ whereas for a bending rigidity dominated device,

this value is expected to be around $2.08 f_0$.^{21,22,28} To further confirm the plate-like behaviour of the NCD resonators, we measured the resonance frequencies of higher-order eigenmodes. Here we observe, for the second mode, resonance frequencies at $1.91 f_0$ to $2.06 f_0$ (Figs. 6.3(b) and (c)), which is in agreement with the expected value for a resonator in the plate limit.

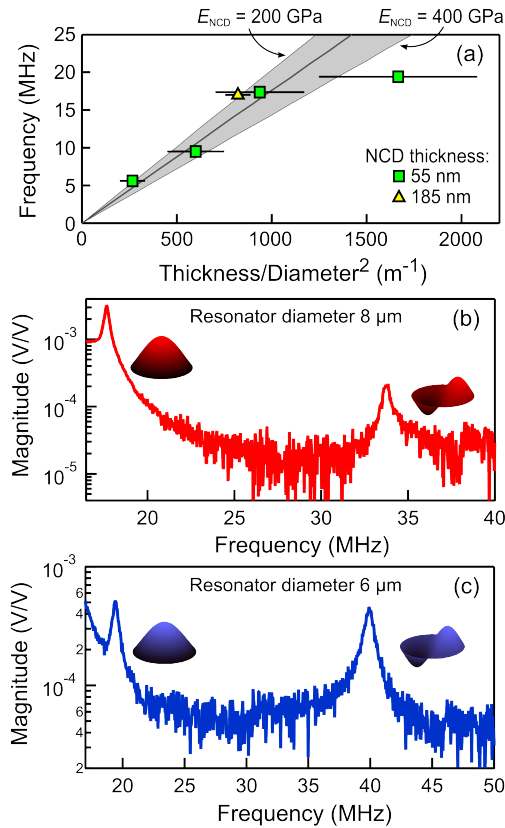


Figure 6.3: (a) Measured resonance frequency as a function of the (resonator) thickness and hole diameter (on a pre-patterned SiO₂ substrate) for the NCD mechanical resonators. The central solid line indicates the calculated resonance frequency with $E = 304 \text{ GPa}$, $\rho = 3500 \text{ kg.m}^{-3}$ and $\nu = 0.12$ (Equation 6.1). Resonance spectra displaying the fundamental and first higher order modes of a 55 nm thick NCD resonator with a diameter of 8 μm (b) and 6 μm (c).

6.4 Conclusion

In summary, we demonstrate the fabrication of NCD-based mechanical resonators by means of a lithography-free fabrication technique based on an all-dry elastomeric stamping. As our stamping technique does not require traditional electron-beam or photolithography followed by wet-chemical processing and critical point drying, it significantly reduces the cost and the complexity of the manufacturing process. Moreover, this process can be performed in 10 - 15 min with a 100 % yield (no collapsed resonators). The fabricated NCD-based resonators display fundamental resonance frequencies in the range of 5 - 20 MHz and Q -factors of 40 - 155 in vacuum at room temperature. The lithography-free fabrication process presented here can be employed to manufacture NCD resonators for fundamental nanomechanics studies as well as to integrate them to more complex pre-designed electronic devices. Furthermore, this process could be modified to exploit current nanoimprint batch fabrication to manufacture NCD resonators at an industrial scale in an efficient and cost-effective way.

References

- ¹ H. G. Craighead, *Science* **290**, 1532-1535 (2000).
- ² K. L. Ekinci, *Small* **1**, 786-797 (2005).
- ³ R. S. Sussmann, *CVD Diamond for Electronic Devices and Sensors*. (Wiley Publications, West Sussex, UK, 2009).
- ⁴ J. Isberg, J. Hammersberg, E. Johansson, T. Wikstrom, D. J. Twitchen, A. J. Whitehead, S. E. Coe, and G. A. Scarsbrook, *Science* **297**, 1670-1672 (2002).
- ⁵ E. A. Ekimov, V. A. Sidorov, E. D. Bauer, N. N. Mel'nik, N. J. Curro, J. D. Thompson, and S. M. Stishov, *Nature* **428**, 542-545 (2004).
- ⁶ C. E. Nebel, D. Shin, B. Rezek, N. Tokuda, H. Uetsuka, and H. Watanabe, *J. R. Soc. Interface* **4**, 439-461 (2007).
- ⁷ O. A. Williams, *Diamond Relat. Mater.* **20**, 621-640 (2011).
- ⁸ P. Rath, S. Khasminskaya, C. Nebel, C. Wild, and W. H. P. Pernice, *Nature Communications* **4**, 1690 (2013).
- ⁹ A. Boisen, *Nat. Nanotechnol.* **4**, 404-405 (2009).
- ¹⁰ J. P. Spatz, *Nature Materials* **4**, 115-116 (2005).
- ¹¹ K. C. Schwab and M. L. Roukes, *Phys. Today* **58**, 36-42 (2005).
- ¹² J. Fritz, M. K. Baller, H. P. Lang, H. Rothuizen, P. Vettiger, E. Meyer, H. J. Guntherodt, C. Gerber, and J. K. Gimzewski, *Science* **288**, 316-318 (2000).
- ¹³ S. Shivaraman, R. A. Barton, X. Yu, J. Alden, L. Herman, M. V. S. Chandrashekar, J. Park, P. L. McEuen, J. M. Parpia, H. G. Craighead, and M. G. Spencer, *Nano Lett.* **9**, 3100-3105 (2009).
- ¹⁴ M. Imboden, O. A. Williams, and P. Mohanty, *Appl. Phys. Lett.* **102**, 103502 (2013).
- ¹⁵ A. V. Sumant, O. Auciello, R. W. Carpick, S. Srinivasan, and J. E. Butler, *MRS Bull.* **35**, 281-288 (2010).
- ¹⁶ Y. Tao, J. M. Boss, B. A. Moores, and C. L. Degen, *Nature Communications* **5**, 3638 (2014).

- ¹⁷ A. D. O'Connell, M. Hofheinz, M. Ansmann, R. C. Bialczak, M. Lenander, E. Lucero, M. Neeley, D. Sank, H. Wang, M. Weides, J. Wenner, J. M. Martinis, and A. N. Cleland, *Nature* **464**, 697-703 (2010).
- ¹⁸ J. M. Pirkkalainen, S. U. Cho, J. Li, G. S. Paraoanu, P. J. Hakonen, and M. A. Sillanpaa, *Nature* **494**, 211-215 (2013).
- ¹⁹ A. Gaidarzhy, M. Imboden, P. Mohanty, J. Rankin, and B. W. Sheldon, *Appl. Phys. Lett.* **91**, 203503 (2007).
- ²⁰ L. Sekaric, J. M. Parpia, H. G. Craighead, T. Feygelson, B. H. Houston, and J. E. Butler, *Appl. Phys. Lett.* **81**, 4455-4457 (2002).
- ²¹ R. A. Barton, B. Ilic, A. M. van der Zande, W. S. Whitney, P. L. McEuen, J. M. Parpia, and H. G. Craighead, *Nano Lett.* **11**, 1232-1236 (2011).
- ²² A. Castellanos-Gomez, R. van Leeuwen, M. Buscema, H. S. J. van der Zant, G. A. Steele, and W. J. Venstra, *Adv. Mater.* **25**, 6719-6723 (2013).
- ²³ O. A. Williams, O. Douheret, M. Daenen, K. Haenen, E. Osawa, and M. Takahashi, *Chem. Phys. Lett.* **445**, 255-258 (2007).
- ²⁴ J. S. Bunch, A. M. van der Zande, S. S. Verbridge, I. W. Frank, D. M. Tanenbaum, J. M. Parpia, H. G. Craighead, and P. L. McEuen, *Science* **315**, 490-493 (2007).
- ²⁵ L. Jay Guo, *Adv. Mater.* **19**, 495-513 (2007).
- ²⁶ a) TEM Grids at Ted Pella, Incorporation: http://www.tedpella.com/grids_html/silicon-nitride-hole.htm; b) Microfilters at Aquamarijn Micro Filtration: http://www.aquamarijn.nl/ms_research.php#high_porosity.
- ²⁷ J. Lee, Z. H. Wang, K. L. He, J. Shan, and P. X. L. Feng, *ACS Nano* **7**, 6086-6091 (2013).
- ²⁸ T. Wah, *J. Acoust. Soc. Am.* **34**, 275-281 (1962).
- ²⁹ J. Wang, J. E. Butler, D. S. Y. Hsu, and C. T. C. Nguyen, *Proceedings: IEEE International Conference on Micro Electro Mechanical Systems* 657-660 (2002).

³⁰ J. Philip, P. Hess, T. Feygelson, J. E. Butler, S. Chattopadhyay, K. H. Chen, and L. C. Chen, *J. Appl. Phys.* **93**, 2164-2171 (2003).

Appendix A

Supplementary Information
Chapter 2

Section 1

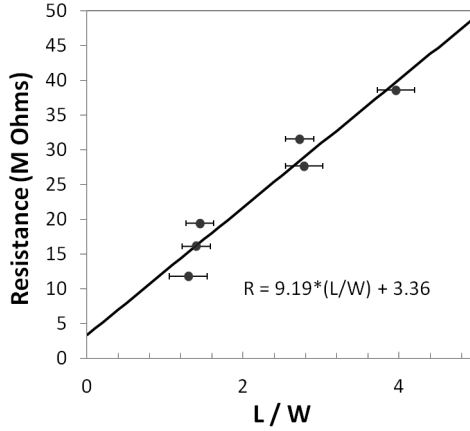


Figure S1: Plot of the surface resistance versus the distance between the contacts (length)/diameter of the contacts (width) in a H_2 -treated undoped film.

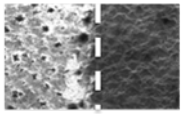
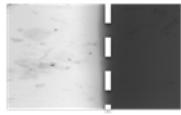
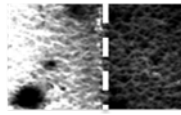
The electrical characterization of oxygen plasma-treated i.e., O-terminated and (same film later) H_2 -treated i.e., H-terminated undoped CVD film was done to measure the surface resistance. The H_2 -treated film was kept under ambient conditions for more than a day before electrical measurements. The electrical contacts on the film surface were achieved using silver paint. The characterization was carried out using a 2-probe technique consisting of a probe station and a Keithley 2100 used in a 2-wire resistance mode (resistance measuring range: 100Ω - $100 M\Omega$). In all cases, the oxygen plasma-treated film showed surface resistance higher than $10 G\Omega$ (the maximum measurable resistance with our setup). The same film on H-termination displayed resistance in the range of 10 - $40 M\Omega$ (Fig. S1), which shows that our H_2 -treated films exhibit surface conductivity on air exposure. By performing 2-probe measurements for different spacing between the probes, one can subtract the contact resistance and determine the surface resis-

tance, here ~ 3.4 and ~ 9.2 $M\Omega$, respectively. The surface resistance value was found to be in reasonable agreement with the values reported in the literature.¹

Section 2

The results of water contact angle (WCA) measurements to analyze the surface wetting properties and scanning electron microscopy (SEM) to visualize the electron affinity of the surfaces are shown in Table SI.

Table SI: Summary of WCA and SEM results for doped (commercial) and undoped (in-house) sample for H_2 treatment at ~ 850 $^\circ C$ and atmospheric pressure with a gas flow ~ 525 ml/min and ~ 50 ml/min.

H_2 treatment	~ 525 ml/min	~ 50 ml/min	~ 50 ml/min
Sample type	Doped	Undoped	Doped
WCA	$85 \pm 9^\circ$	$88 \pm 7^\circ$	$87 \pm 8^\circ$
SEM			

In supplement to the water contact angle and SEM measurements a micro-droplet condensation experiment was carried out on a diamond sample with two different areas, i.e., H_2 -treated and UV/ozone-treated, prepared in a similar way than the samples for SEM analysis. The sample was continuously inspected under the optical microscope with $10\times$ magnification while simply exhaling over the diamond surface, which leads to condensation of water micro-droplets. The qualitative difference between hydrophobicity and hydrophilicity can be easily distinguished by the condensation pattern; on hydrophobic surfaces the water droplets are smaller

and spherical, whereas on hydrophilic surfaces the water droplets are coalesced forming large area puddles (Fig. S2).

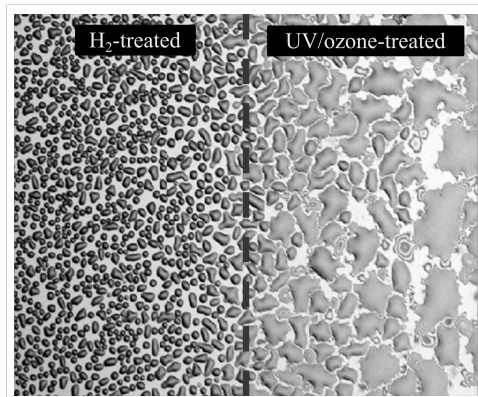


Figure S2: Optical image of micro-droplet condensation on H_2 -treated and UV/ozone-treated undoped (in-house) CVD diamond film. The dashed line (guide to the eye) indicates the boundary between the H_2 -treated and UV/ozone-treated portion on the same film.

Section 3

Point scans were carried out at three different locations of treated and untreated (before any annealing treatment, purchased from Element 6 company) CVD diamond films. The X-ray spot size was $400\ \mu\text{m}$. Each survey measurement was averaged over 10 scans at pass energy of 200 eV. Figure S3(a), (b) and (c) show the presence of Si 2p peak in addition to C 1s and O 1s peaks for all three surface treatments. No Si 2p peak was observed on an untreated film (Fig. S3(d)). The atomic percentage of C, O and Si obtained from XPS measurements are shown in Table SII. The atomic percentage ratio for Si:O was $\sim 1:2$ for H plasma treatment and H_2 -treatment, which suggests that this oxygen could be bound to the detected silicon as SiO_2 . For UV/ozone treatment, this ratio was found to be higher i.e., $\sim 1:3$ due to additional oxygen groups. The absence of any Si impurities on an untreated film suggest that

these impurities could be coming from the walls of the quartz tube reactor, which was heated upto ~ 850 °C during high-temperature annealing.

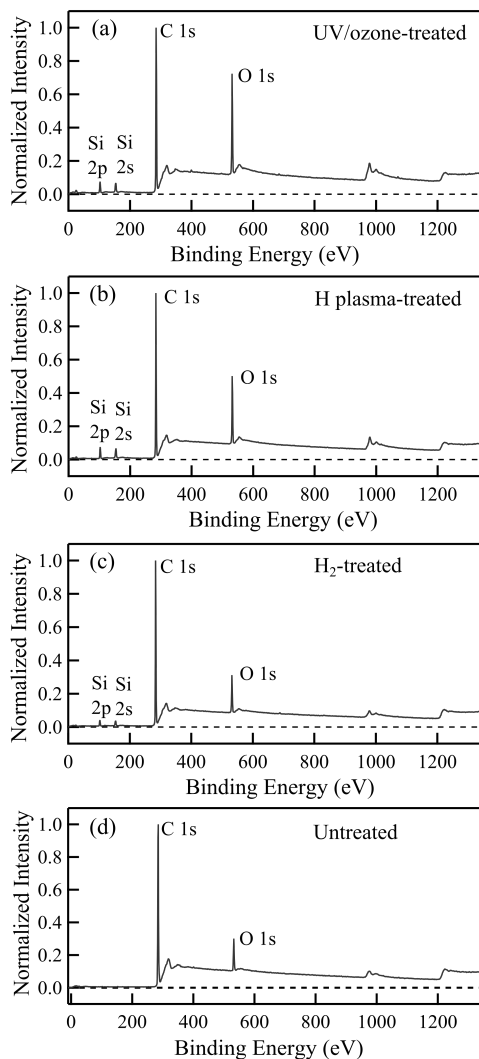


Figure S3: XPS survey scan spectra of undoped (in-house) CVD diamond film treated with (a) UV/ozone, (b) H plasma, (c) H₂-treatment at ~ 850 °C and atmospheric pressure and (d) doped (commercial) CVD diamond film before any annealing treatment.

Table SII: Atomic % of C, O and Si for UV/ozone, H plasma and H₂-treatment at ~850 °C and atmospheric pressure.

Surface treatment	Atomic % C	Atomic % O	Atomic % Si
UV/ozone	73.85	19.40	6.75
H plasma	76.67	15.52	7.81
H ₂ -treatment	85.67	9.85	4.47

Section 4

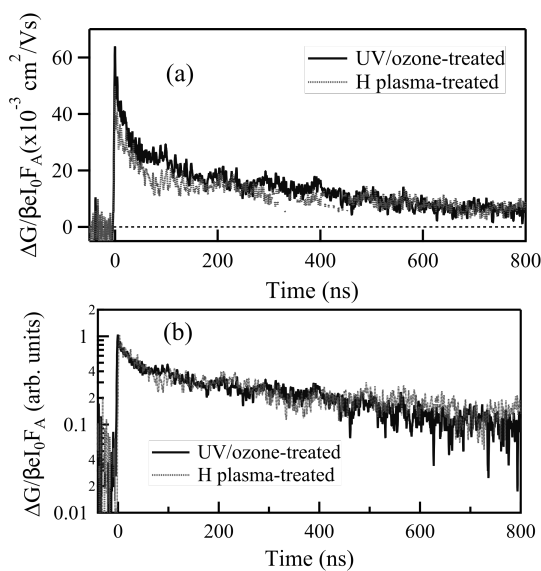


Figure S4: (a) Photoconductance transient for H plasma-treated (light curve) and UV/ozone-treated (dark curve) boron-doped (in-house) CVD diamond film measured using TRMC technique. (b) Normalized photoconductance transient showing charge carrier lifetime data.

The boron-doped (in-house) CVD diamond film used for TRMC measurements had boron-to-carbon concentration ratio of ~3000 ppm making it metallic in nature.² Photoconductance magnitudes,

given by the maximum value of $\Delta G/\beta eI_0F_A$, obtained for H plasma-treated (light curve, $\sim 0.05 \text{ cm}^2/\text{Vs}$) and UV/ozone-treated (dark curve, $\sim 0.06 \text{ cm}^2/\text{Vs}$) boron-doped diamond film were found to be similar (Fig. S4(a)). In addition, the carrier lifetimes of photo-generated charges were also found to be similar (Fig. S4(b)). In contrast to the undoped films, the similar results for two different terminations on the doped films could be attributed to fermi level pinning due to high boron doping in the film.

References

- ¹ P. Hubik, J. J. Mares, H. Kozak, A. Kromka, B. Rezek, J. Kristofik, and D. Kindl, *Diamond Relat. Mater.* **24**, 63-68 (2012).
- ² J. J. Mares, M. Nesladek, P. Hubik, D. Kindl, and J. Kristofik, *Diamond Relat. Mater.* **16**, 1-5 (2007).

Appendix B

Supplementary Information
Chapter 5

We have investigated the nature of the electron transport in the diamond devices with nanogaps by recording current vs. voltage (I - V) characteristics at different temperatures. Figure S1 shows this temperature dependence for one of the devices with a nanogap. The I - V characteristics look similar at all the temperatures except for a slight decrease in current at lower temperatures. The observed differences in the I - V characteristics are consistent with tunneling behavior as the main transport mechanism through the gap.¹

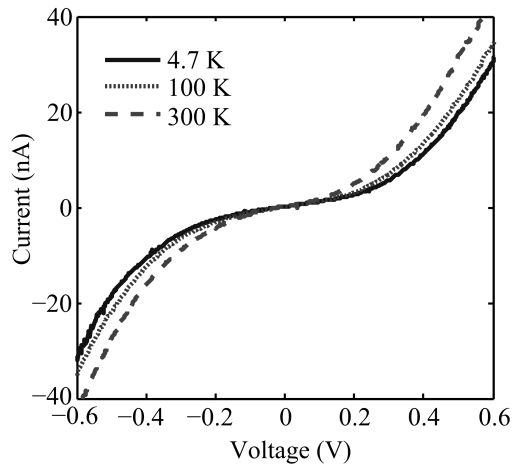


Figure S1: Current vs. voltage characteristics of a diamond device with a nanogap at different temperatures.

Reference

- ¹ J. G. Simmons, J. Appl. Phys. **34**, 1793-1803 (1963).

Appendix C

Supplementary Information
Chapter 6

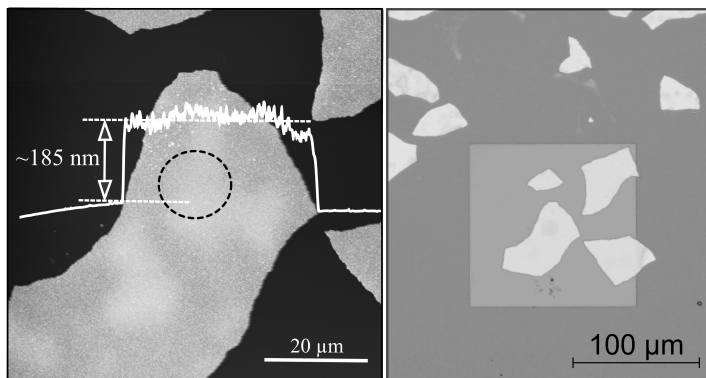


Figure S1: Tapping-mode atomic force microscopy (AFM) was performed to estimate the thickness of the NCD flakes using a Digital Instruments D3100 AFM with a standard silicon cantilever (spring constant of 40 N/m and tip curvature < 10 nm). Left panel shows the AFM image and the thickness profile of a NCD resonator/layer. The thickness was found to be 185 nm. The dotted circle in the AFM image represents the location of a pre-patterned hole (diameter: 15 μm) on the SiO_2 substrate. Right panel shows the corresponding optical image of the NCD resonator suspended over the hole (diameter: 15 μm) on SiO_2 substrate.

Summary

Natural diamond is one of the most rare and precious gemstones known to mankind. In addition, it is also known for its exceptional material properties including extreme heat conducting capacity at room temperature, chemical inertness to aqueous environments and excellent electrical insulation that are interesting to both fundamental as well as applied sciences. These attractive properties of natural diamond and the difficulty of its mining led to the production of synthetic diamond via high pressure and high temperature (HPHT) and chemical vapour deposition (CVD) techniques. Gradually, with the utilization and improvements of these techniques, there has been a growing interest in the research community to exploit the superior material properties of diamonds. In this thesis, the chemical, electronic and mechanical properties of CVD diamonds were investigated to mainly elucidate their fundamental properties and also to evaluate their commercial applicability in terms of processing.

The thesis is divided into three sections: the surface chemistry (Chapter 2), the bulk (opto)electronic properties (Chapters 3, 4 and 5) and the mechanical properties of thin films (Chapter 6). All chapters deal with CVD diamond, typically nanocrystalline diamond (NCD).

In Chapter 2 a new approach to hydrogen terminate diamond films is introduced. The hydrogenated NCD films were prepared by heating the samples to ~ 850 °C in the presence molecular hydrogen gas at atmospheric pressure. At the elevated temperature, diamond reacts with hydrogen gas molecules producing a hydrogenated surface. The resulting surfaces were analysed with surface wettability, electron affinity, elemental composition, photo-conductivity, and redox studies and were found to be very similar with those prepared using the standard hydrogen plasma technique. Unlike high vacuum techniques, our method can be easily scaled up to fabricate cost-effective hydrogenated diamond for industry.

In Chapter 3 hydrogen and oxygen surface-terminated NCD films were studied by the contactless time-resolved microwave conductivity (TRMC) technique and X-ray photoelectron spectroscopy (XPS). For undoped films it was observed that the surface termination affects the photoconductive properties in terms of charge mobility and carrier lifetime, while doped films showed no dependency on the surface termination. The results are explained by differences in band bending profile as a result of differences in surface termination and the presence of doping. Analysis of the valence band spectra obtained by XPS suggested that upon oxidation of undoped NCD the surface Fermi level shifts (towards an increased work function), leading to different types of band bending at the diamond/air interface in the presence of a water film. In contrast, the Fermi level for doped NCD does not shift.

Chapter 4 covers the electrical characterization of boron-doped NCD films. To this end, NCD Hall bar geometries were fabricated using standard lithography techniques. These structures were characterized to study their electronic properties such as superconductivity, magneto-resistance and transverse resistance at low temperature (20 mK to 5 K) in the presence of a perpendicular oriented magnetic field. It was observed that at room temperatures the Hall bar structures behave as a normal electrical conductor whereas at low temperature these structures show superconducting

behaviour. In addition, the charge carrier density of $\sim 1.6 \times 10^{21} \text{ cm}^{-3}$ in these films was estimated from the Hall measurements.

Chapter 5 presents a new method to produce nanogaps and hybrid diamond/graphite nanostructures in boron-doped NCD. Nanometer-sized gaps down to $\sim 1 \text{ nm}$ are produced using a feedback-controlled current annealing procedure. The nanogaps were characterized using scanning electron microscopy, electronic transport measurements and Raman spectroscopy. The formation of hybridized diamond/graphite structure was found to take place at the point of maximum heat accumulation.

In Chapter 6 we present an innovative, 15-minute, lithography-free, all-dry elastomeric stamp-transfer technique to fabricate mechanical resonators from diamond films. Using this method, freely suspended diamond drum structures were produced with thicknesses of $\sim 55 \text{ nm}$ and $\sim 185 \text{ nm}$ and diameters from $6 \text{ }\mu\text{m}$ to $15 \text{ }\mu\text{m}$ at 100 % yield, i.e., no collapse of resonators was observed. Their resonance behaviour was characterized using an optical interferometer setup to show their practical applicability.

Samenvatting

Natuurlijke diamant is één van de meest zeldzame en waardevolle edelstenen. Daarnaast staat diamant ook bekend om zijn exceptionele materiaaleigenschappen zoals een hoge warmtegeleiding bij kamertemperatuur, chemische inertie in waterige milieus en uitstekende (elektrische) isolatie-eigenschappen – aantrekkelijk voor zowel fundamentele als toegepaste wetenschap. Deze interessante eigenschappen en de uitdagingen in het winnen van natuurlijk diamant hebben geleid tot de productie van synthetische diamant door middel van technieken die gebruik maken van hoge druk en hoge temperatuur (HPHT) en chemische opdampprocessen (CVD). Het gebruik en de ontwikkeling van deze technieken heeft geleid tot een toenemende interesse in de onderzoeksgemeenschap, die de superieure materiaaleigenschappen van diamant wil exploiteren. In dit proefschrift wordt onderzoek naar chemische, elektrische en mechanische eigenschappen van CVD-diamanten onderzocht, om zo de fundamentele eigenschappen op te helderen, als wel het evalueren van de commerciële toepasbaarheid wat betreft het bewerken van diamant.

Dit proefschrift is verdeeld in drie secties: de oppervlaktechemie (Hoofdstuk 2), de (opto)elektronische eigenschappen van de bulk (Hoofdstukken 3, 4 en 5) en de mechanische eigenschappen van

dunne diamantfilms (Hoofdstuk 6). Alle hoofdstukken betreffen CVD-diamanten, en wel speciaal nanokristallijn diamant (NCD).

Hoofdstuk 2 introduceert een nieuwe methode om diamantfilms te termineren met waterstof. De hydrogeneerde NCD-films zijn bereid door ze te verhitten tot ~ 850 °C in de aanwezigheid van moleculair waterstofgas bij atmosferische druk. Bij de verhoogde temperatuur reageert diamant met waterstofgasmoleculen, waarbij een gehydrogeneerd oppervlak ontstaat. De gemodificeerde oppervlakken werden vervolgens geanalyseerd met oppervlaktebevochtigings-, elektronenaffiniteits-, elementen-compositie-, fotoconductiviteits- en redox-studies. De geanalyseerde oppervlakken werden zeer vergelijkbaar bevonden aan oppervlakken die werden bereid met de standaard waterstof-plasmatechniek. In tegenstelling tot hoog-vacuümtechnieken kan onze techniek eenvoudig worden opgeschaald om zo gehydrogeneerde diamanten te produceren voor industriële toepassingen op een kostenefficiënte manier.

In Hoofdstuk 3 worden waterstof- en zuurstof-oppervlakgetermineerde NCD films bestudeerd door *time-resolved microwave conductivity* (TRMC) en *X-ray photoelectron spectroscopy* (XPS). De oppervlakteterminatie van niet-gedoteerde films bleek de fotogeleidende eigenschappen te beïnvloeden met betrekking tot de mobiliteit van de lading en de levensduur van de ladingsdrager, terwijl gedoteerde films geen afhankelijkheid toonden in oppervlakteterminatie. De resultaten zijn verklaard door verschillen in de zogenaamde bandbuigingsprofielen als gevolg van verschillen in oppervlakteterminatie en de aanwezigheid van dotering. Analyse van de valentiebandenspectra verkregen door XPS suggereert dat de Fermi-niveaus van geoxideerde, niet-gedoteerde NCDs verschuiven (richting een grotere werkfunctie) wat, in de aanwezigheid van een waterfilm, tot verscheidene bandbuigingen aan het diamant/lucht-grensvlak leidt.

Hoofdstuk 4 bestrijkt de elektrische karakterisatie van boor-gedoteerde NCD-films. Daartoe zijn zogenaamde NCD *Hall bar*

structuren gefabriceerd met standaard lithografische technieken. De elektronische eigenschappen van deze structuren, waaronder supergeleiding, de magnetische weerstand en de transversale weerstand zijn gekarakteriseerd bij lage temperaturen (20 mK tot 5 K) in de aanwezigheid van een loodrecht georiënteerd magnetisch veld. Bij lage temperaturen gedragen de structuren zich als normale elektronische geleiders, terwijl deze structuren bij lage temperaturen supergeleidend gedrag vertonen.

In Hoofdstuk 5 wordt een nieuwe methode gepresenteerd voor het produceren van nano-openingen en hybride diamant/grafiet-nanostructuren in boorgedoteerde NCD films. Via een teruggekoppelde, stroomgedreven warmtebehandelingsmethode zijn nanometergrote openingen tot ~ 1 nm geproduceerd. De nano-openingen zijn bestudeerd door middel van rasterelektronenmicroscopie, elektrische transportmetingen en Raman spectroscopie. Op het punt van de maximale warmteophoping werd de meeste vorming van gehybridiseerde diamant/grafiet-structuren gevonden.

In Hoofdstuk 6 presenteren we een innovatieve, vijftien minuten durende, lithografie-vrije, droge, elastomere stempeloverdracht-methode voor het fabriceren van mechanische resonatoren vanuit diamantfilms. Met deze methode zijn vrijhangende diamanten drumstructuren geproduceerd met diktes van ~ 55 nm en ~ 185 nm, en diameters van $6 \mu\text{m}$ tot $15 \mu\text{m}$. Doordat er geen instorting van resonatoren werd geobserveerd, was de opbrengst 100%. Om de praktische toepassingen te tonen, is met behulp van een optische interferometer het resonantiegedrag bestudeerd.

List of Publications

2009 – 2014

5. **V. Seshan**, R. van Leeuwen, W. J. Venstra, B. Schneider, S. D. Janssens, M. Nešládek, K. Haenen, E. J. R. Sudhölter, L. C. P. M. de Smet, H. S. J. van der Zant, G. A. Steele, and A. Castellanos-Gomez “*Stamp-transfer fabrication of nanocrystalline diamond mechanical resonators*” In preparation.
4. **V. Seshan**, D. H. K. Murthy, A. Castellanos-Gomez, S. Sachdeva, H. A. Ahmad, S. D. Janssens, W. Janssen, K. Haenen, H. S. J. van der Zant, E. J. R. Sudhölter, T. J. Savenije, and L. C. P. M. de Smet “*Contactless photo-conductance study on undoped and doped nanocrystalline diamond films*” Submitted.
3. **V. Seshan**, D. Ullien, A. Castellanos-Gomez, S. Sachdeva, D. H. K. Murthy, T. J. Savenije, H. A. Ahmad, T. S. Nunnery, S. D. Janssens, K. Haenen, M. Nešládek, H. S. J. van der Zant, E. J. R. Sudhölter, and L. C. P. M. de Smet “*Hydrogen termination of CVD diamond films by high-temperature annealing at atmospheric pressure*” *The Journal of Chemical Physics*, 2013 138(23): 234707.

2. **V. Seshan**, C. R. Arroyo, A. Castellanos-Gomez, F. Prins, M. L. Perrin, S. D. Janssens, K. Haenen, M. Nesládek, E. J. R. Sudhölter, L. C. P. M. de Smet, H. S. J. van der Zant, and D. Dulic “*Current-induced nanogap formation and graphitization in boron-doped diamond films*” Applied Physics Letters, 2012 101(19): 195106.

2009 – prior to this thesis

1. M. Diez, P. Mela, **V. Seshan**, M. Möller, and M. C. Lensen “*Nanomolding of PEG-based hydrogels with sub-10 nm resolution*” Small, 2009 5(23): 2756.

Acknowledgements

My experience as a Ph.D. researcher has been a memorable one. This journey has been possible only because of the help and support of the people mentioned in this section.

First and foremost, I am deeply grateful to my bosses Ernst, Herre and Louis for considering me for this top job. I thank them very much for all the freedom they gave me to explore my ideas during the course of research and timely support throughout my research. It has been a wonderful learning experience for me. Being part of the two different research groups OMI and MED gave me a lot of opportunities to gain, discuss and broaden my knowledge.

I would also like to thank Prof. Hamers, Prof. Hanson, Prof. Lemay, Prof. Schmidt-Ott and Prof. Wagner for being part of my thesis defense committee.

My research on diamond was carried out in close collaboration with Ken, Milos, Stoffel and Wiebke from Hasselt University, Belgium. I thank them for their unlimited supply of diamond samples and also for sharing their inputs towards our joint publications.

While carrying out the TRMC project, I worked extensively with Murthy and Tom from the OM group and I am very grateful to them for their help. I learnt a lot in the area of opto-electronics through our never-ending discussions. I also thank Maria, Ruben

and Sandeep for their assistance with the TRMC and spectrophotometer setups.

My special thanks go to all the support staff for their kindness and diligence. From the OMI group: Astrid (I will always remember your help on the tough issues with my residence permit. Thank you very much), Duco (for the interesting and sometimes crazy discussions on diamonds), Karin, Lars, Louw, Marian and Piet. From the MED group: Dorin, Erika, Irma, Maria, Mascha and Ron. I also thank the VLL staff members Marc, Marco and Roel for their help in the cleanroom.

I enjoyed my research the most when I discussed and worked with my OMI and MED group members. So I am thankful to my former and current OMI members: Aernout, Aldo (for the discussions during lunch and coffee breaks), Anping, Cristian, Daniela (for all your assistance with the experiments, all the best with your thesis), Judith (for all chats we had, best wishes for your thesis), Marleen (for countless discussions and help when needed), Michel (for initial cleanroom training), Miguel, Stefan, Sumit, Thomas, William, Wolter and Zhen. From the MED group, I thank the former members: Anne (for the nice hospitality in Grenoble), Alexander, Carlos (I enjoyed our team work and marathon measurement sessions), Christian (for helping me during my initial period in MED), Diana (for all our discussions on diamond and non-diamond topics), Harold, Hidde, Jeppe, Jos (it was fun organizing movie nights with you), Menno, and Samir (for helping with the measurements and all the discussions we had) and the current members: Anna, Ben (for being an amazing officemate, all the best with your thesis), Ben B, Enrique, Gary, Joshua, Max, Michael, Michele (for being always ready to help me), Riccardo, Ronald (for organizing movie nights together), Sal, Sander, Vibhor and Warner. Andres and Ferry, special thanks to you for being my mentors throughout my Ph.D. and motivating me to strive harder when the going got tougher. I also thank all the other people at OMI, MED and ASM for their support.

Life outside research was equally fun with my friends. My thanks to Amit G, Chidambaresan, Gopakumar, Gopika, Girish, Jayakrishnan, Lalit, Mallesh, Mohan, Nishant, Purvil, Rajat, Renuka, Sairam, Sushil, Uday, Vasu, Venkataraman K and Vijayender. I also thank Joop and Ria for providing a pleasant accommodation at Bagijnhof 70.

I am thankful to Celeste, Jaap, Mia and all the other TMOTH members for their continual support in improving my public speaking skills.

Special thanks to Abrar, Amit P, Aniruddha, Arvind B, Deepak, Gunjan, John, Kalyan, Keyur, Krishna, Parag, Prasanth, Punit, Rajorshi, Ravi, Sandeep M, Shriniwas, Shreyas, Shyam, Sunil, Tejas and Venkatraman I for all their help, support and much needed company during tough times in the past and present.

Lastly, I would like to thank my parents, my brother, my grandmother, my uncle, my aunty and my numerous cousins for the years of unlimited love and support they have given me. More importantly, thank you for being there for me all the time.

Venkatesh Seshan
June 2014

About the author



Venkatesh Seshan was born in Mannargudi (India) on September 27 and brought up in Mumbai (India). He completed his Bachelor's degree in Electronics from the University of Mumbai in 2002. After working in industry for more than 3 years, Venkatesh enrolled for Masters at Chalmers University of Technology (Sweden) in 2006 and graduated with a degree in Nanoscale Science and Technology in 2008. During his Masters, Venkatesh carried out his thesis work at the DWI-RWTH University (Germany) and completed an internship at the Indian Institute of Technology (India).

In 2009, he joined the groups of Prof. Ernst Sudhölter and Prof. Herre van der Zant at the Delft University of Technology (The Netherlands) as a Ph.D. researcher on diamond material.